Decoherence and gate performance of coupled solid-state qubits

Markus J. Storcz* and Frank K. Wilhelm

Sektion Physik and CeNS, Ludwig-Maximilians-Universität, Theresienstrasse 37, 80333 München, Germany
(Received 16 December 2002; published 23 April 2003; publisher error corrected 28 April 2003)

Solid-state quantum bits are promising candidates for the realization of a *scalable* quantum computer. However, they are usually strongly limited by decoherence due to the many extra degrees of freedom of a solid-state system. We investigate a system of two solid-state qubits that are coupled via $\sigma_z^{(i)} \otimes \sigma_z^{(j)}$ type of coupling. This kind of setup is typical for *pseudospin* solid-state quantum bits such as charge or flux systems. We evaluate decoherence properties and gate quality factors in the presence of a common and two uncorrelated baths coupling to σ_z, respectively. We show that at low temperatures, uncorrelated baths do degrade the gate quality more severely. In particular, we show that in the case of a common bath, optimum gate performance of a controlled-PHASE gate can be reached at very low temperatures, because our type of coupling commutes with the coupling to the decoherence, which makes this type of coupling interesting as compared to previously studied proposals with $\sigma_y^{(i)} \otimes \sigma_y^{(j)}$ coupling. Although less pronounced, this advantage also applies to the controlled-NOT gate.

I. INTRODUCTION

Quantum computation has been shown to perform certain tasks much faster than classical computers [1–3]. Presently, very mature physical realizations of this idea originate in atomic physics, optics, and nuclear magnetic resonance. These systems are phase coherent in abundance, however, scaling up the existing few-qubit systems is not straightforward. Solid-state quantum computers have the potential advantage of being arbitrarily scalable to large systems of many qubits [4–6]. Their most important drawback is the coupling to the many degrees of freedom of a solid-state system. Even though recently, there has been fast progress in improving the decoherence properties of experimentally realized solid-state quantum bits [7–11], this remains a formidable task.

Quite a lot is known about decoherence properties of single solid-state qubits, see, e.g., Refs. [12–14], but much less is known about systems of two or more coupled qubits [15–17]. However, only for systems of at least two qubits, the central issue of entanglement can be studied. The physically available types of qubit coupling can be classified as Heisenberg-type exchange that is typical for real spin-1/2 systems, and Ising-type coupling, which is characteristic for *pseudospin* setups, where the computational degrees of freedom are not real spins. In the latter, the different spin components typically correspond to distinct variables, such as charge and flux [10,18] whose couplings can and have to be engineered on completely different footing. Previous work [16,17] presented the properties of a system of two coupled solid-state qubits that are coupled via $\sigma_y^{(i)} \otimes \sigma_y^{(j)}$ type coupling as proposed in Ref. [14] as the current-current coupling of superconducting charge quantum bits.

On the other hand, many systems such as inductively coupled flux qubits [6], capacitively coupled charge qubits [7,8], and other pseudospin systems [19] are described by a

$\sigma_z^{(i)} \otimes \sigma_z^{(j)}$ Ising-type coupling. This indicates that the computational basis states are coupled, which, i.e., in the case of flux qubits are magnetic fluxes, whereas $\sigma_{x/y}$ are electric charges. The σ_z observable is a natural way of coupling, because it is typically easy to couple to. We will study a two qubit-system coupled this way that is exposed to Gaussian noise coupling to σ_z, the "natural" observable. This example accounts for the crucial effect of electromagnetic noise in superconducting qubits. We will compare both the cases of noise that affects both qubits in a correlated way and the case of uncorrelated single-qubit errors. We determine the decoherence properties of the system by application of the well-known Bloch-Redfield formalism and determine quality factors of a controlled-NOT (CNOT) gate for both types of errors and feasible parameters of the system.

II. MODEL HAMILTONIAN

We model the Hamiltonian of a system of two qubits, coupled via Ising-type coupling. Each of the two qubits is a two-state system that is described in pseudospin notation by the single-qubit Hamiltonian [13]

$$\mathbf{H}_{sq} = -\frac{1}{2}\epsilon\hat{\sigma}_z - \frac{1}{2}\Delta\hat{\sigma}_x, \tag{1}$$

where ϵ is the energy bias and Δ the tunnel matrix element. The coupling between the qubits is determined by an extra term in the Hamiltonian $\mathbf{H}_{qq} = -(K/2)\hat{\sigma}_z^{(1)} \otimes \hat{\sigma}_z^{(2)}$ that represents e.g., inductive interaction (directly or via flux transformer) in the case of flux qubits [6,20]. Thus, the complete two-qubit Hamiltonian in the absence of a dissipative environment reads

$$\mathbf{H}_{2qb} = \sum_{i=1,2}\left(-\frac{1}{2}\epsilon_i\hat{\sigma}_z^{(i)} - \frac{1}{2}\Delta_i\hat{\sigma}_x^{(i)}\right) - \frac{1}{2}K\hat{\sigma}_z^{(1)}\hat{\sigma}_z^{(2)}. \tag{2}$$

The dissipative (bosonic) environment is conveniently modeled as either a common bath or two distinct baths of har-

*Electronic address: storcz@theorie.physik.uni-muenchen.de

monic oscillators, coupling to the σ_z components of the two qubits. This approach universally models baths which produce *Gaussian* fluctuations, such as the noise from linear electrical circuits. An example for a situation described by a common bath is long correlation length electromagnetic noise from the experimental environment or noise generated or picked up by coupling elements such as flux transformers [6]. Short correlation length radiation or local readout and control electronics coupling to individual qubits [13] might be described as coupling to two uncorrelated baths of harmonic oscillators.

One should note that if the number of qubits is increased to more than two, there might also occur dissipative effects that neither affect all qubits nor only a single qubit, but rather a cluster of qubits, thus, enhancing the complexity of our considerations [21].

In the case of two uncorrelated baths, the full Hamiltonian reads

$$\mathbf{H}_{2qb}^{2b} = \sum_{i=1,2} \left(-\frac{1}{2}\epsilon_i \hat{\sigma}_z^{(i)} - \frac{1}{2}\Delta_i \hat{\sigma}_x^{(i)} + \frac{1}{2}\hat{\sigma}_z^{(i)}\hat{X}^{(i)} \right)$$
$$- \frac{1}{2}K\hat{\sigma}_z^{(1)}\hat{\sigma}_z^{(2)} + \mathbf{H}_{B_1} + \mathbf{H}_{B_2}, \quad (3)$$

where each qubit couples to its own, distinct harmonic oscillator bath $\mathbf{H}_{B_i}$, $i=1,2$, via the coupling term $\hat{\sigma}_z^{(i)}\hat{X}^{(i)}$, $i=1,2$, that bilinearly couples a qubit to the collective bath coordinate $\hat{X}^{(i)} = \zeta\Sigma_\nu\lambda_\nu x_\nu$. We again sum over the two qubits. In the case of two qubits coupled to one common bath, we model our two-qubit system with the Hamiltonian

$$\mathbf{H}_{2qb}^{1b} = -\frac{1}{2}\sum_{i=1,2}(\epsilon_i\hat{\sigma}_z^{(i)} + \Delta_i\hat{\sigma}_x^{(i)}) - \frac{1}{2}K\hat{\sigma}_z^{(1)}\hat{\sigma}_z^{(2)}$$
$$+ \frac{1}{2}(\hat{\sigma}_z^{(1)} + \hat{\sigma}_z^{(2)})\hat{X} + \mathbf{H}_B, \quad (4)$$

where $\mathbf{H}_B$ denotes one common bath of harmonic oscillators.

The appropriate starting point for our further analysis is the singlet/triplet basis, consisting of $|\uparrow\uparrow\rangle := (1,0,0,0)^T$, $(1/\sqrt{2})(|\uparrow\downarrow\rangle + |\downarrow\uparrow\rangle) := (0,1,0,0)^T$, $|\downarrow\downarrow\rangle := (0,0,1,0)^T$, and the singlet state $(1/\sqrt{2})(|\uparrow\downarrow\rangle - |\downarrow\uparrow\rangle) := (0,0,0,1)^T$. In the case of flux qubits, the $\uparrow$ and $\downarrow$ states correspond to clockwise and counterclockwise currents respectively.

In this basis, the undamped Hamiltonian $\mathbf{H}_{2qb}$, Eq. (2), of the two-qubit system assumes the matrix form

$$\mathbf{H}_{2qb} = -\frac{1}{2}\begin{pmatrix} \epsilon+K & \eta & 0 & -\Delta\eta \\ \eta & -K & \eta & \Delta\epsilon \\ 0 & \eta & K-\epsilon & \Delta\eta \\ -\Delta\eta & \Delta\epsilon & \Delta\eta & -K \end{pmatrix}, \quad (5)$$

with $\epsilon = \epsilon_1 + \epsilon_2$, $\eta = (\Delta_1 + \Delta_2)/\sqrt{2}$, $\Delta\eta = (\Delta_1 - \Delta_2)/\sqrt{2}$, and $\Delta\epsilon = \epsilon_1 - \epsilon_2$. From now on, for simplicity, we concentrate on the case of equal parameter settings, $\Delta_1 = \Delta_2$ and $\epsilon_1 = \epsilon_2$.

If we now also express the coupling to the dissipative environment in this basis, we find in the case of coupling to two uncorrelated distinct baths that

$$\mathbf{H}_{2qb}^{2b} = -\frac{1}{2}\begin{pmatrix} \epsilon-s+K & \eta & 0 & 0 \\ \eta & -K & \eta & -\Delta s \\ 0 & \eta & K-\epsilon+s & 0 \\ 0 & -\Delta s & 0 & -K \end{pmatrix}, \quad (6)$$

with $s = X_1 + X_2$ and $\Delta s = X_1 - X_2$. Here, the bath mediates transitions between the singlet and triplet states, the singlet is not a protected subspace.

In the case of two qubits with equal parameters that are coupled to one common bath, we obtain the matrix

$$\mathbf{H}_{2qb}^{1b} = -\frac{1}{2}\begin{pmatrix} \epsilon-s+K & \eta & 0 & 0 \\ \eta & -K & \eta & 0 \\ 0 & \eta & K-\epsilon+s & 0 \\ 0 & 0 & 0 & -K \end{pmatrix}, \quad (7)$$

where $s = 2X$ and $\Delta s = 0$. One directly recognizes that compared to Eq. (6) in this case, thermalization to the singlet state is impeded, because Eq. (7) is block diagonal in the singlet and triplet subspaces. The singlet and triplet are completely decoupled from each other, and in the case of one common bath the singlet is also completely decoupled from the bath and thus, protected from dissipative effects. Therefore, a system in contact with one common bath that is prepared in the singlet state will never experience any decoherence effects. The singlet state is a decoherence free subspace (DFS) [22], although a trivial, one-dimensional one.

III. EIGENENERGIES AND EIGENSTATES OF THE TWO-QUBIT HAMILTONIAN

We calculate exact analytical eigenvalues and eigenvectors of the unperturbed two-qubit system Hamiltonian in the aforementioned symmetric case of Eq. (5), which reads

$$\mathbf{H}_{2qb} = -\frac{1}{2}\begin{pmatrix} \epsilon+K & \eta & 0 & 0 \\ \eta & -K & \eta & 0 \\ 0 & \eta & K-\epsilon & 0 \\ 0 & 0 & 0 & -K \end{pmatrix}. \quad (8)$$

This Hamiltonian is block diagonal and the largest block, the triplet, is three dimensional, i.e., it can be diagonalized using Cardano's formula. Details of that calculation are given in Ref. [23]. The case of nonidentical qubits is more easily handled numerically.

In the following, $|E1\rangle$, $|E2\rangle$, $|E3\rangle$, and $|E4\rangle$ denote the eigenstates of the two-qubit system. The eigenenergies of the unperturbed Hamiltonian (8) depend on the three parameters K, ϵ, and η. Fig. 1 displays the eigenenergies in more detail for typical experimentally accessible values. The values that are chosen for the parameters ϵ, η, and K in Fig. 1 correspond to what can be reached in flux qubits. They typically assume values of a few GHz resembling the parameters
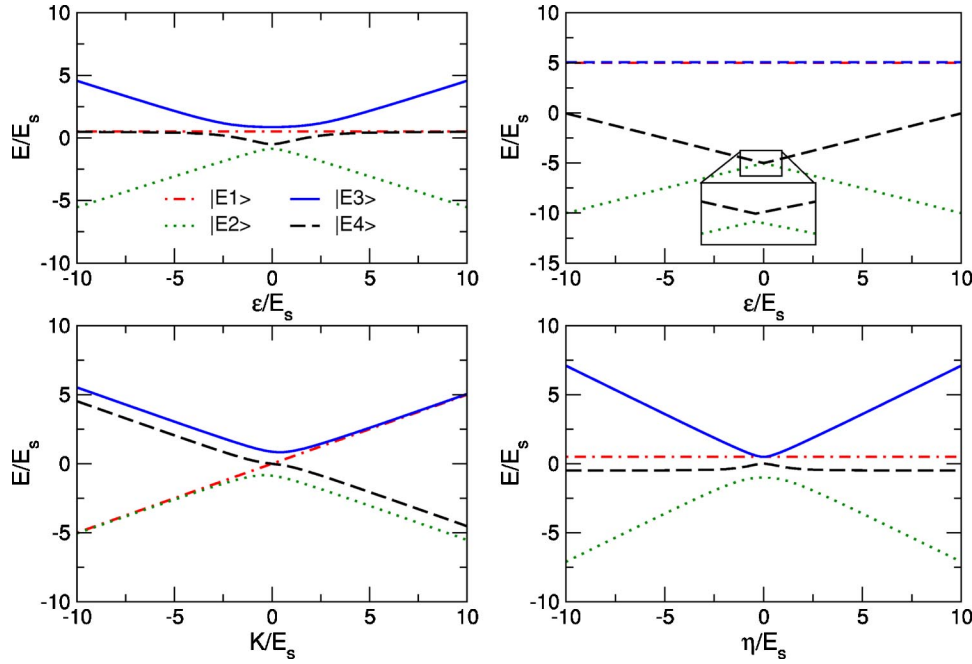
FIG. 1. Plot of the eigenenergies of the eigenstates $|E1\rangle$, $|E2\rangle$, $|E3\rangle$, and $|E4\rangle$. From upper left to lower right: (1) $K=\eta=E_s$ and ϵ is varied, (2) $K=10E_s$, $\eta=E_s$, and ϵ is varied; the inset resolves the avoided level crossing due to the finite transmission amplitude η; (3) $\eta=\epsilon=E_s$ and K is varied; (4) $K=\epsilon=E_s$ and η is varied.

of known single- and two-qubit experiments in Delft [13] and at MIT [24]. Therefore, we will use a characteristic energy scale E_s, which is typically $E_s=1$ GHz. The corresponding scales are $t_s=1$ ns, $\omega_s=2\pi\times1$ GHz, and $T_s=\nu_s(h/k_B)=4.8\times10^{-2}$ K. Panel (1) shows that for large values of ϵ, two of the eigenenergies are degenerate (namely, for $\epsilon\gg\eta,K$ the states $|E1\rangle$ and $|E4\rangle$ equal the states $(1/\sqrt{2})(|\uparrow\downarrow\rangle-|\downarrow\uparrow\rangle)$ and $(1/\sqrt{2})(|\uparrow\uparrow\rangle+|\downarrow\downarrow\rangle)$, hence the eigenenergies are degenerate) while near zero energy bias (magnetic frustation $f=1/2$) all four eigenenergies might be distinguished. Note also that, therefore, at zero energy bias, the transition frequency $\omega_{14}=-\omega_{41}$ has a local *maximum*, which, as will be shown below, can only be accessed via nonsymmetric driving.

If K is set to a big positive value corresponding to large ferromagnetic coupling [Fig. 1, panel (2), $K=10E_s$], the Hamiltonian (8) is nearly diagonal and, hence, the eigenstates in good approximation are equal to the singlet/triplet basis states. In this case, $|E3\rangle$ equals the triplet state $(1/\sqrt{2})(|\uparrow\downarrow\rangle+|\downarrow\uparrow\rangle)$, $|E2\rangle$ and $|E4\rangle$ equal $|\uparrow\uparrow\rangle$ and $|\downarrow\downarrow\rangle$, respectively, for positive values of ϵ. For large negative values of ϵ, the two states $|E2\rangle$ and $|E4\rangle$ become equal $|\downarrow\downarrow\rangle$ and $|\uparrow\uparrow\rangle$ with a pseudo-spin-flip between clockwise and counterclockwise rotating currents at $\epsilon=0$ when going from positive to negative ϵ. In the case of large ferromagnetic coupling, the ground state tends towards the superposition $(1/\sqrt{2})(|\uparrow\uparrow\rangle+|\downarrow\downarrow\rangle)$. Panel (2) shows that only for ϵ equal to zero, both $|E2\rangle=|\uparrow\uparrow\rangle$ ($|E2\rangle=|\downarrow\downarrow\rangle$, for negative ϵ) and $|E4\rangle=|\downarrow\downarrow\rangle$ ($|E4\rangle=|\uparrow\uparrow\rangle$, for negative ϵ) have the same energies (which one would expect if the $-(1/2)K\sigma_z^{(1)}\sigma_z^{(2)}$ term in the Hamiltonian dominates), because if ϵ is increased, the $\epsilon_i\hat{\sigma}_z^{(i)}$ ($i=1,2$) terms in the Hamiltonian change the energy.

For large antiferromagnetic coupling, $|-K|\gg\epsilon,\Delta$ the states $|\uparrow\downarrow\rangle$ and $|\downarrow\uparrow\rangle$ are favorable. In this limit, the ground state tends towards $(1/\sqrt{2})(|\uparrow\downarrow\rangle+|\downarrow\uparrow\rangle)$ and the energy splitting between $(1/\sqrt{2})(|\uparrow\downarrow\rangle+|\downarrow\uparrow\rangle)$ and $(1/\sqrt{2})(|\uparrow\downarrow\rangle-|\downarrow\uparrow\rangle)$ vanishes asymptotically, leaving the ground state nearly degenerate.

From Fig. 1, panel (3), one directly recognizes that the singlet eigenenergy crosses the triplet spectrum, which is a consequence of the fact that the singlet does not interact with any triplet states. At zero energy bias (magnetic frustration $f=1/2$, for a flux qubit), none of the eigenstates equal one of the triplet basis states (e.g., as observed for a large energy bias ϵ), they are rather nontrivial superpositions. This is elucidated further in the following paragraph. The inset of panel (2) depicts the level anticrossing between the eigenenergies of the two states $|E2\rangle$ and $|E4\rangle$ due to quantum tunneling.

In general, the eigenstates are a superposition of singlet/triplet states. Figure 2 shows how singlet/triplet states combine into eigenstates for different qubit parameters. The first eigenstate $|E1\rangle$ equals $(1/\sqrt{2})(|\uparrow\downarrow\rangle-|\downarrow\uparrow\rangle)$ for all times while the other eigenstates $|E2\rangle$, $|E3\rangle$, and $|E4\rangle$ are in general superpositions of the singlet/triplet basis states. For large values of $|\epsilon|$, the eigenstates approach the singlet/triplet) basis states. In particular, at typical working points, where $\epsilon\approx5\Delta$ [13], the eigenstates already nearly equal the singlet/triplet basis states. Hence, although the anticrossing described above corresponds to the anticrossing used in Refs. [9,25] to demonstrate Schrödinger's cat states, *entanglement* is prevalent away from the degeneracy point. For an experimental proof, one still would have to show that one has successfully prepared coherent couplings by spectroscopically tracing the energy spectrum. Note that, for clarity, in
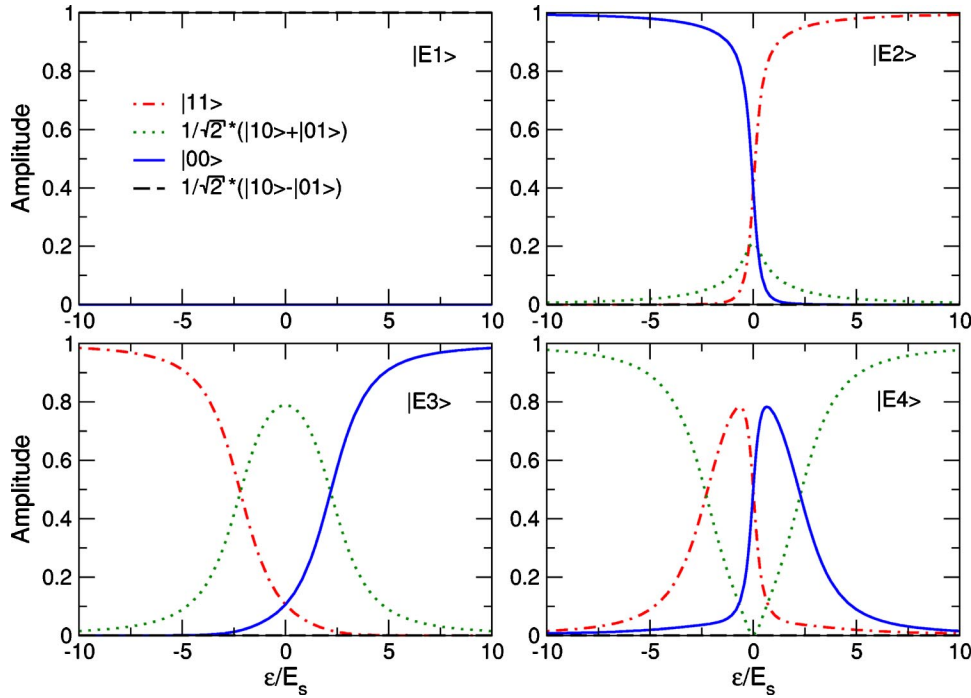
FIG. 2. Plot of the amplitude of the different singlet (triplet) states of which the eigenstates denoted by $|E1\rangle$, $|E2\rangle$, $|E3\rangle$, and $|E4\rangle$ are composed for the four eigenstates. In all plots ϵ is varied, and K and η are fixed to E_s.

Fig. 2, the interqubit coupling strength K is fixed to a rather large value of E_s that also sets the width of the anticrossing, which potentially can be very narrow.

Spectroscopy

As a first technological step towards demonstrating coherent manipulation of qubits, usually the transition frequencies between certain energy levels are probed [9,25], i.e., the energy *differences* between the levels. Figures 3 and 4 depict the transition frequencies between the four eigenstates. The transition frequencies are defined as $\omega_{nm} = (E_n - E_m)/\hbar$ and

$\omega_{nm} = -\omega_{mn}$. The transitions between the singlet state $|E1\rangle$ and the triplet states are forbidden in the case of one common bath, due to the special symmetries of the Hamiltonian (4), if the system is driven collectively through a time-dependent energy bias $\epsilon_1(t) = \epsilon_2(t)$. However, in the case of two distinct baths, the environment can mediate transitions between the singlet and the triplet states.

Not all transition frequencies have local minima at $\epsilon = 0$. The frequencies ω_{41} and ω_{34} have local maxima at zero energy bias ϵ. This can already be inferred from Fig. 1, panel (1), the energy of the eigenstate $|E4\rangle$ has a local minimum at $\epsilon = 0$. Similarly, the substructure of ω_{34} can be understood from Fig. 1: the frequency ω_{34} has a local maximum at ϵ
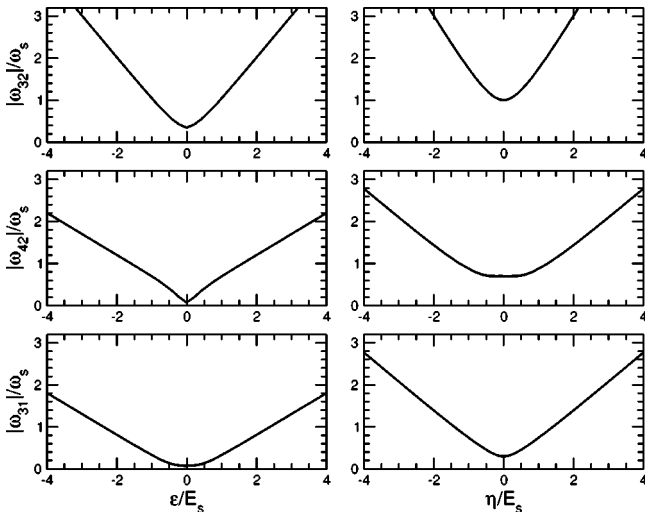

FIG. 3. Plot of the absolute value of the transition frequencies ω_{32}, ω_{42}, and ω_{31}. In the left column $K = \eta = 0.2E_s$ and ϵ is varied. In the right column, $K = 0.2E_s$, $\epsilon = E_s$, and η is varied.
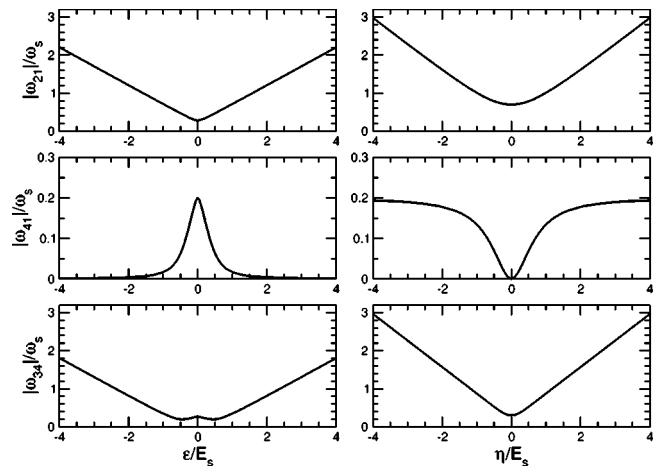

FIG. 4. Plot of the transition frequencies ω_{21}, ω_{41}, and ω_{34}. In the left column, $K = \eta = 0.2E_s$ and ϵ is varied. In the right column, $K = 0.2E_s$, $\epsilon = E_s$, and η is varied.

$=0$, because of the local minimum of the eigenenergy of the state $|E4\rangle$. First, if ϵ is increased, the level spacing of $|E4\rangle$ and $|E3\rangle$ decreases. Then, for larger values of ϵ, the level spacing of $|E4\rangle$ and $|E3\rangle$ increases again. Thus, the structure observed for ω_{34} around $\epsilon=0$ emerges in Fig. 4.

IV. BLOCH-REDFIELD FORMALISM

In order to describe decoherence in the weak damping limit, we use the Bloch-Redfield Formalism [26]. It provides a systematic way of finding a set of coupled master equations which describes the dynamics of the reduced (i.e., the reservoir coordinates are traced out) density matrix for a given system in contact with a dissipative environment and has recently been shown to be numerically equivalent to the more elaborate path-integral scheme [27]. The Hamiltonian of our two-qubit system in contact with a dissipative environment, Eqs. (3) and (4), has the generic "system+bath" form

$$\mathbf{H}_{op}(t)=\mathbf{H}_{2qb}+\mathbf{H}_B+\mathbf{H}_{int}, \qquad (9)$$

where $\mathbf{H}_B$ is a bath of harmonic oscillators and $\mathbf{H}_{int}$ inherits the coupling to a dissipative environment. In our case, the effects of driving are not investigated. In Born approximation and when the system is only weakly coupled to the environment, Bloch-Redfield theory provides the following set of equations for the reduced density matrix ρ describing the dynamics of the system [28,29]:

$$\dot{\rho}_{nm}(t)=-i\omega_{nm}\rho_{nm}(t)-\sum_{kl}R_{nmk\ell}\rho_{k\ell}(t), \qquad (10)$$

where $\omega_{nm}=(E_n-E_m)/\hbar$, and $\max_{n,m,k,\ell}|\mathrm{Re}(R_{nmk\ell})|$ $<\min_{n\neq m}|\omega_{nm}|$ must hold. The Redfield relaxation tensor $R_{nmk\ell}$ comprises the dissipative effects of the coupling of the system to the environment. The elements of the Redfield relaxation tensor are given through golden rule rates [28]

$$R_{nmk\ell}=\delta_{\ell m}\sum_r \Gamma_{nrrk}^{(+)}+\delta_{nk}\sum_r \Gamma_{\ell rrm}^{(-)}$$
$$-\Gamma_{\ell mnk}^{(+)}-\Gamma_{\ell mnk}^{(-)}. \qquad (11)$$

A. Two qubits coupled to two distinct baths

We now evaluate the Golden rule expressions in Eq. (11) in the case of two qubits, each coupled to a distinct harmonic oscillator bath. Here, $\tilde{H}_I(t)=\exp(iH_Bt/\hbar)H_I\exp(-iH_Bt/\hbar)$ denotes the coupling between system and bath in the interaction picture, and the bracket denotes thermal average of the bath degrees of freedom. Writing down all contributions gives

$$\Gamma_{\ell mnk}^{(+)}=\hbar^{-2}\int_0^\infty dt e^{-i\omega_{nk}t}\langle e^{[i(H_{B_1}+H_{B_2})t/\hbar]}$$
$$\times(\sigma_{z,\ell m}^{(1)}\otimes\hat{X}^{(1)}+\sigma_{z,\ell m}^{(2)}\otimes\hat{X}^{(2)})e^{[-i(H_{B_1}+H_{B_2})t/\hbar]}$$
$$\times(\sigma_{z,nk}^{(1)}\otimes\hat{X}^{(1)}+\sigma_{z,nk}^{(2)}\otimes\hat{X}^{(2)})\rangle, \qquad (12)$$

where $\sigma_{z,nm}^{(i)}$ $(i=1,2)$ are the matrix elements of $\hat{\sigma}_z^{(i)}$ with respect to the eigenbasis of the unperturbed Hamiltonian (8) and likewise for $\Gamma_{\ell mnk}^{(-)}$.

We assume Ohmic spectral densities with a Drude cutoff. This is a realistic assumption, i.e., for electromagnetic noise [13] and leads to integrals in the rates which are tractable by the residue theorem. The cutoff frequency ω_c for the spectral functions of the two qubits is typically assumed to be the largest frequency in the problem, this is discussed further in Sec. IV E,

$$J_1(\omega)=\frac{\alpha_1\hbar\omega}{1+\dfrac{\omega^2}{\omega_c^2}} \quad \text{and} \quad J_2(\omega)=\frac{\alpha_2\hbar\omega}{1+\dfrac{\omega^2}{\omega_c^2}}. \qquad (13)$$

The dimensionless parameter α describes the strength of the dissipative effects that enter the Hamiltonian via the coupling to the environment, described by s and Δs. In order for the Bloch-Redfield formalism, which involves a Born approximation in the system-bath coupling, to be valid, we have to assume $\alpha_{1/2}\ll 1$. After tracing out over the bath degrees of freedom, the rates read

$$\Gamma_{\ell mnk}^{(+)}=\frac{1}{8\hbar}[\Lambda^1 J_1(\omega_{nk})+\Lambda^2 J_2(\omega_{nk})][\coth(\beta\hbar\omega_{nk}/2)-1]$$
$$+\frac{i}{4\pi\hbar}[\Lambda^2 M^-(\omega_{nk},2)+\Lambda^1 M^-(\omega_{nk},1)] \qquad (14)$$

with $\Lambda^1=\Lambda_{\ell mnk}^1=\sigma_{z,\ell m}^{(1)}\sigma_{z,nk}^{(1)}$, $\Lambda^2=\Lambda_{\ell mnk}^2=\sigma_{z,\ell m}^{(2)}\sigma_{z,nk}^{(2)}$, and

$$M^\pm(\Omega,i)=\mathcal{P}\int_0^\infty d\omega\frac{J_i(\omega)}{\omega^2-\Omega^2}[\coth(\beta\hbar\omega/2)\Omega\pm\omega],$$
$$(15)$$

here $\mathcal{P}$ denotes the principal value. Likewise,

$$\Gamma_{\ell mnk}^{(-)}=\frac{1}{8\hbar}[\Lambda^1 J_1(\omega_{\ell m})+\Lambda^2 J_2(\omega_{\ell m})][\coth(\beta\hbar\omega_{\ell m}/2)+1]$$
$$+\frac{i}{4\pi\hbar}[\Lambda^2 M^+(\omega_{\ell m},2)+\Lambda^1 M^+(\omega_{\ell m},1)]. \qquad (16)$$

The rates $\Gamma_{\ell mnk}^{(+)}$ and $\Gamma_{\ell mnk}^{(-)}$ might be inserted into Eq. (11) to build the Redfield tensor. Note, here, that for $\omega_{nk}\to 0$, and $\omega_{\ell m}\to 0$ respectively, the real part of the rates (which is responsible for relaxation and dephasing) is of value $\Gamma_{\ell mnk}^{(+)}=\Gamma_{\ell mnk}^{(-)}=(1/4\beta\hbar)[\sigma_{z,\ell m}^{(1)}\sigma_{z,nk}^{(1)}\alpha_1+\sigma_{z,lm}^{(2)}\sigma_{z,nk}^{(2)}\alpha_2]$.

To solve the set of differential equations (10), it is convenient to collapse ρ into a vector. In general, the Redfield equations (10) without driving are solved by an ansatz of the type $\rho(t)=B\exp(\tilde{R}t)B^{-1}\rho(0)$, where $\tilde{R}$ is a diagonal matrix. The entries of this diagonal matrix are the eigenvalues of the Redfield tensor (11), written in matrix form, including the dominating term $i\omega_{nm}$ [cf. Eq. (10)]. Here, the reduced density matrix $\rho=(\rho_{11},\ldots,\rho_{44})^T$ is written as a vector. The
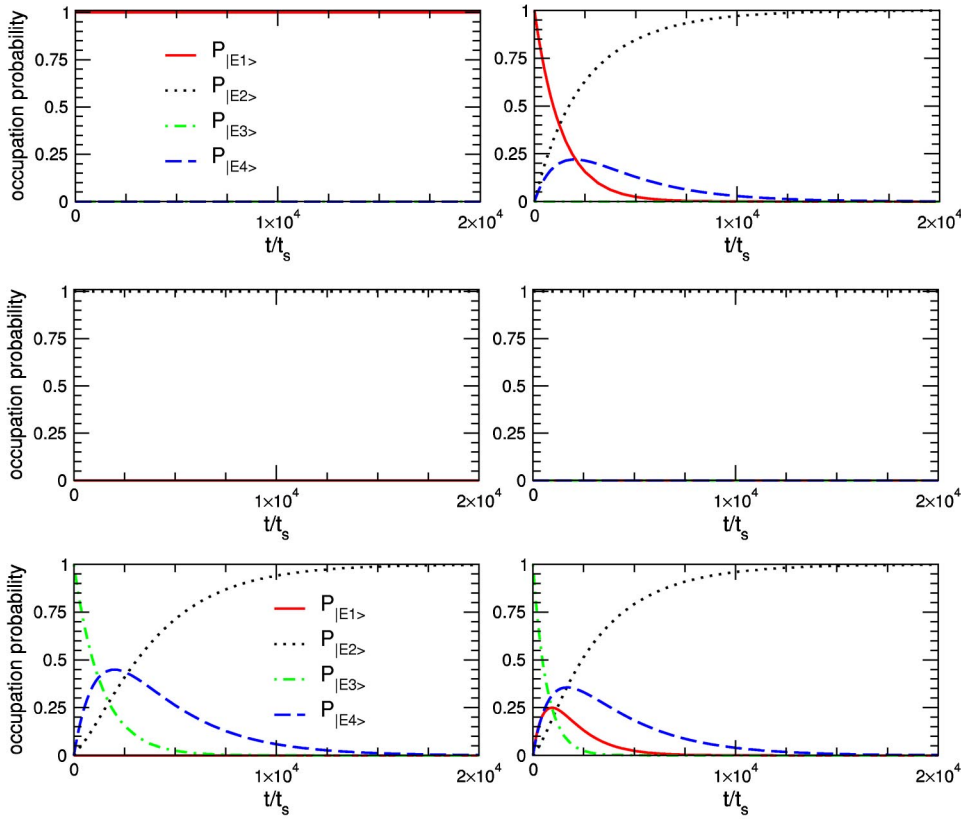
FIG. 5. Plot of the occupation probability of the four eigenstates $|E1\rangle$, $|E2\rangle$, $|E3\rangle$, and $|E4\rangle$ for initially starting in one of the eigenstates $|E1\rangle$ (first row), $|E2\rangle$ (second row), or $|E3\rangle$ (third row) at $T=0$. The left column illustrates the case of two qubits coupling to one common bath and the right column the case of two qubits coupling to two distinct baths. The energies K, ϵ, and η are all fixed to E_s. The characteristic time scale t_s is $t_s=1/\nu_s$.

matrix B describes the basis change to the eigenbasis of $\tilde{R}$, in which $\tilde{R}$ has diagonal form.

B. Two qubits coupled to one common bath

For the case of two qubits coupled to one common bath, we perform the same calculation as in the preceding section, which leads to expressions for the rates analogous to Eqs. (16)

$$\Gamma^{(+)}_{\ell mnk} = \frac{1}{8\hbar}\Lambda J(\omega_{nk})[\coth(\beta\hbar\omega_{nk}/2)-1] + \frac{i\Lambda}{4\pi\hbar}$$

$$\times \mathcal{P}\int_0^\infty d\omega \frac{J(\omega)}{\omega^2-\omega_{nk}^2}[\coth(\beta\hbar\omega/2)\omega_{nk}-\omega],$$

(17)

with $\Lambda = \Lambda_{\ell mnk} = \sigma^{(1)}_{z,\ell m}\sigma^{(1)}_{z,nk} + \sigma^{(1)}_{z,\ell m}\sigma^{(2)}_{z,nk} + \sigma^{(2)}_{z,\ell m}\sigma^{(1)}_{z,nk} + \sigma^{(2)}_{z,\ell m}\sigma^{(2)}_{z,nk}$ and

$$\Gamma^{(-)}_{\ell mnk} = \frac{1}{8\hbar}\Lambda J(\omega_{\ell m})[\coth(\beta\hbar\omega_{\ell m}/2)+1] + \frac{i\Lambda}{4\pi\hbar}$$

$$\times \mathcal{P}\int_0^\infty d\omega \frac{J(\omega)}{\omega^2-\omega_{\ell m}^2}[\coth(\beta\hbar\omega/2)\omega_{\ell m}+\omega].$$

(18)

The difference between the rates for the case of two distinct baths (14) and (16) are the two extra terms $\sigma^{(1)}_{z,\ell m}\sigma^{(2)}_{z,nk}$ and $\sigma^{(2)}_{z,\ell m}\sigma^{(1)}_{z,nk}$. They originate when tracing out the bath degrees of freedom. In the case of one common bath, there is only one spectral function, which we also assume to be Ohmic $J(\omega)=(\alpha\hbar\omega)/(1+\omega^2/\omega_c^2)$. For $\omega_{nk}\rightarrow 0$, and $\omega_{\ell m}\rightarrow 0$, respectively, the real part of the rates is of the value $\Gamma^{(+)}_{\ell mnk}=\Gamma^{(-)}_{\ell mnk}=(\alpha/4\beta\hbar)\Lambda$, for $\omega_{\ell m},\omega_{nk}\rightarrow 0$.

C. Dynamics of coupled flux qubits with dissipation

The dissipative effects affecting the two-qubit system lead to decoherence, which manifests itself in two ways. The system experiences energy relaxation on a time scale $\tau_R=\Gamma_R^{-1}$ (Γ_R is the sum of the relaxation rates of the four diagonal elements of the reduced density matrix; $\Gamma_R=-\Sigma_n\Theta_n$ and Θ_n are the eigenvalues of the matrix that consists of the tensor elements $R_{n,m,n,m}$, $n,m=1,\ldots,4$), called relaxation time, into a thermal mixture of the system's energy eigenstates. Therefore, the diagonal elements of the reduced density matrix decay to the value given by the Boltzmann factors. The quantum coherent dynamics of the system are superimposed on the relaxation and decay on a usually shorter time scale $\tau_{\varphi_{ij}}=\Gamma_{\varphi_{ij}}^{-1}$ ($i,j=1,\ldots,4;i\neq j$ and $\Gamma_{\varphi_{nm}}=-\mathrm{Re}R^{1b,2b}_{n,m,n,m}$) termed dephasing time. Thus, dephasing causes the off-diagonal terms (coherences) of the reduced density matrix to tend towards zero.

First, we investigate the incoherent relaxation of the two-qubit system out of an eigenstate. At long times, the system is expected to reach thermal equilibrium, $\rho_{eq}=(1/Z)e^{-\beta H}$. Special cases are $T=0$, where ρ_{eq} equals the projector on
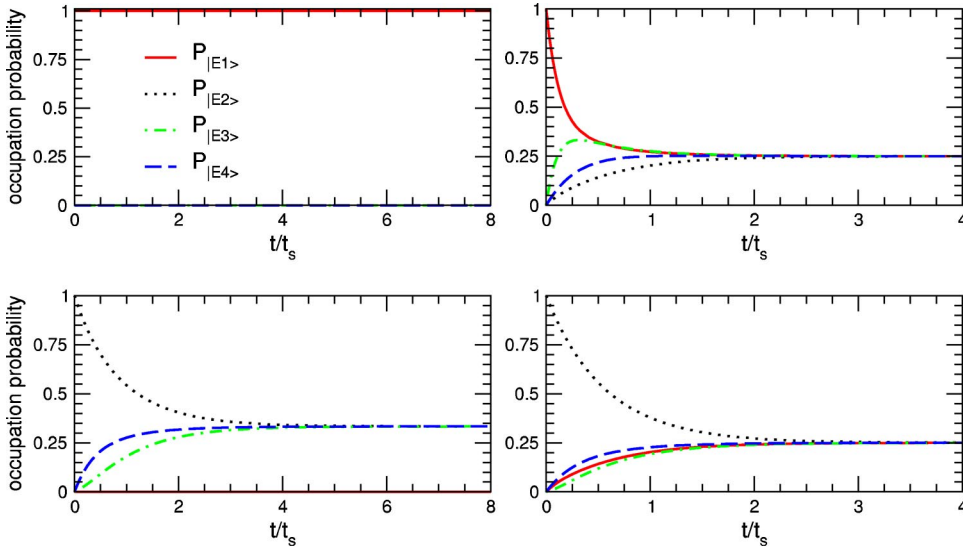
FIG. 6. Plot of the occupation probability of the four eigenstates $|E1\rangle$, $|E2\rangle$, $|E3\rangle$, and $|E4\rangle$ for initially starting in one of the eigenstates $|E1\rangle$ (upper row) or $|E2\rangle$ (lower row) at $T=21T_s$. The left column illustrates the case of two qubits coupling to one common bath and the right column the case of two qubits coupling to two distinct baths. The energies K, ϵ, and η are all fixed to E_s. The characteristic time scale t_s is $t_s=1/\nu_s$.

the ground state and $T\rightarrow\infty$, where all eigenstates are occupied with the same probability, i.e., $\rho_{eq}=(1/4)\hat{1}$. Figures 5 and 6 illustrate the relaxation of the system prepared in one of the four eigenstates for temperatures $T=0$ and $T=21T_s$ respectively. The qubit energies K, ϵ, and η are all set to E_s and α is set to $\alpha=10^{-3}$. From Fig. 1, one recognizes relaxation into the eigenstate $|E2\rangle$, the ground state for this set of parameters.

At low temperatures ($T=0$), we observe that for the case of two distinct uncorrelated baths, a system prepared in one of the four eigenstates always relaxes into the ground state. In the case of two qubits coupling to one common bath, this is not always the case, as can be seen in the upper left panels of Figs. 5 and 6. This can be explained through our previous observation, that the singlet is a protected subspace: Neither the free nor, unlike in the case of distinct baths, the bath-mediated dynamics couple the singlet to the triplet space. Moreover, we can observe that relaxation to the ground state happens by populating intermediate eigenstates with a lower energy than the initial state the system was prepared in at $t=0$ (cf. Fig. 1).

For high temperatures ($T\simeq21T_s$), the system thermalizes into thermal equilibrium, where all eigenstates have equal occupation probabilities. Again, in the case of one common bath, thermalization of the singlet state is impeded and the three eigenstates $|E2\rangle$, $|E3\rangle$ and $|E4\rangle$ have equal occupation probabilites of 1/3 after the relaxation time.

If the system is prepared in a superposition of eigenstates, e.g., $|E3\rangle$ and $|E4\rangle$ as in Fig. 7, which are not in a protected subspace, we observe coherent oscillations between the eigenstates that are damped due to dephasing and after the decoherence time, the occupation probability of the eigenstates is given by the Boltzmann factors. This behavior is depicted in Fig. 7. Here, for $\alpha=10^{-3}$, the cases of $T=0$ and $T=2.1T_s$ are compared. When the temperature is low enough, the system will relax into the ground state $|E2\rangle$, as illustrated by the right column of Fig. 7. Thus, the occupation probability of the state $(1/\sqrt{2})(|E3\rangle+|E4\rangle)$ goes to zero. Here, in the case of zero temperature, the decoherence

times for the case of one common or two distinct baths are of the same order of magnitude. The left column illustrates the behavior when the temperature is increased. At $T=2.1T_s$, the system relaxes into an equally populated state on times much shorter than for $T=0$. For low temperatures, the characteristic time scale for dephasing and relaxation is somewhat shorter for the case of one common bath ($\tau^{1b}/\tau^{2b}\approx0.9$, for $\alpha=10^{-3}$). This can be explained by observing the temperature dependence of the rates shown in Fig. 8. Though for the case of one common bath, two of the dephasing rates are zero at $T=0$, the remaining rates are always slightly bigger for the case of one common bath compared to the case of two distinct baths. If the system is prepared in a general superposition, here $|E3\rangle$ and $|E4\rangle$, nearly all rates become important thus compensating the effect of the two rates that are approximately zero at zero temperature and leading to faster decoherence.

If α and, therefore, the strength of the dissipative effects is increased from $\alpha=10^{-3}$ to $\alpha=10^{-2}$, the observed coherent motion is significantly damped. Variation of α leads to a phase shift of the coherent oscillations, due to renormalization of the frequencies [16]. However, in our case, the effects of renormalization are very small, as discussed in Sec. IV E, and cannot be observed in our plots.

D. Temperature dependence of the rates

Figure 8 displays the dependence of typical dephasing rates and the relaxation rate Γ_R on temperature. These decoherence rates are the inverse decoherence times. The rates are of the same magnitude for the cases of one common bath and two distinct baths. As a notable exception, in the case of one common bath, the dephasing rates $\Gamma_{\varphi_{21}}=\Gamma_{\varphi_{12}}$ go to zero when the temperature is decreased, while all other rates saturate for $T\rightarrow0$. This phenomenon is explained later on. If the temperature is increased from $T_s=(h/k_B)\nu_s=4.8\times10^{-2}$ K, the increase of the dephasing and relaxation rates follows a power-law dependence. It is linear in temperature T with a slope given by the prefactors of the expression in the Red-
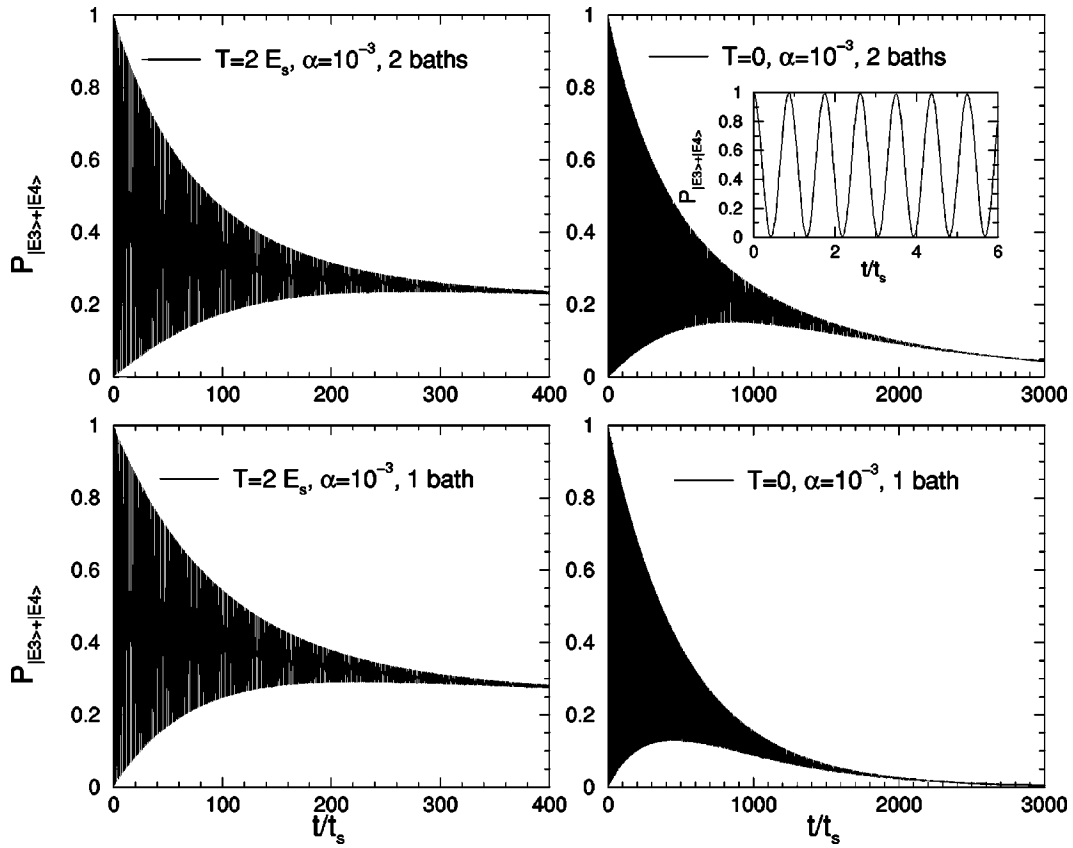
FIG. 7. Plot of the occupation probability $P_{(1/\sqrt{2})(|E3\rangle+|E4\rangle)}(t)$ when starting in the initial state $(1/\sqrt{2})(|E3\rangle+|E4\rangle)$, which is a super-position of eigenstates $|E3\rangle$ and $|E4\rangle$. The first row shows the behavior for two qubits coupling to two uncorrelated baths. The lower row shows the behavior for two qubits coupled to one common bath. The qubit parameters ϵ, η, and K are set to E_s and α is set to $\alpha = 10^{-3}$. The inset resolves the time scale of the coherent oscillations.
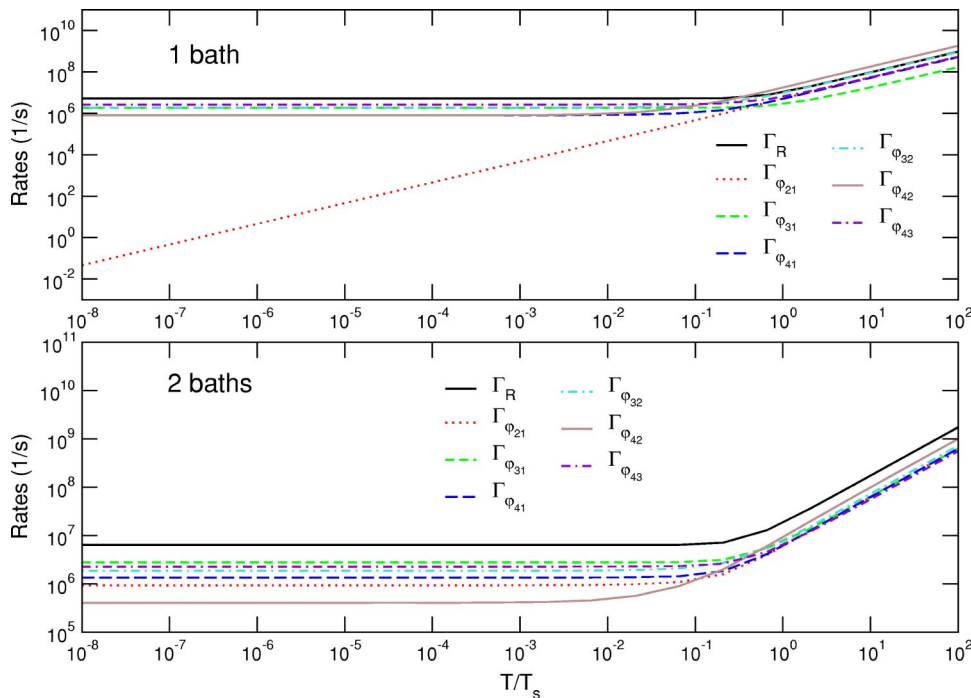

FIG. 8. Log-log plot of the temperature dependence of the sum of the four relaxation rates and selected dephasing rates. Qubit parameters K, ϵ, and η are all set to E_s and $\alpha = 10^{-3}$. The upper panel shows the case of one common bath and the lower panel the case of two distinct baths. At the characteristic temperature of approximately $0.1T_s$, the rates increase very steeply.
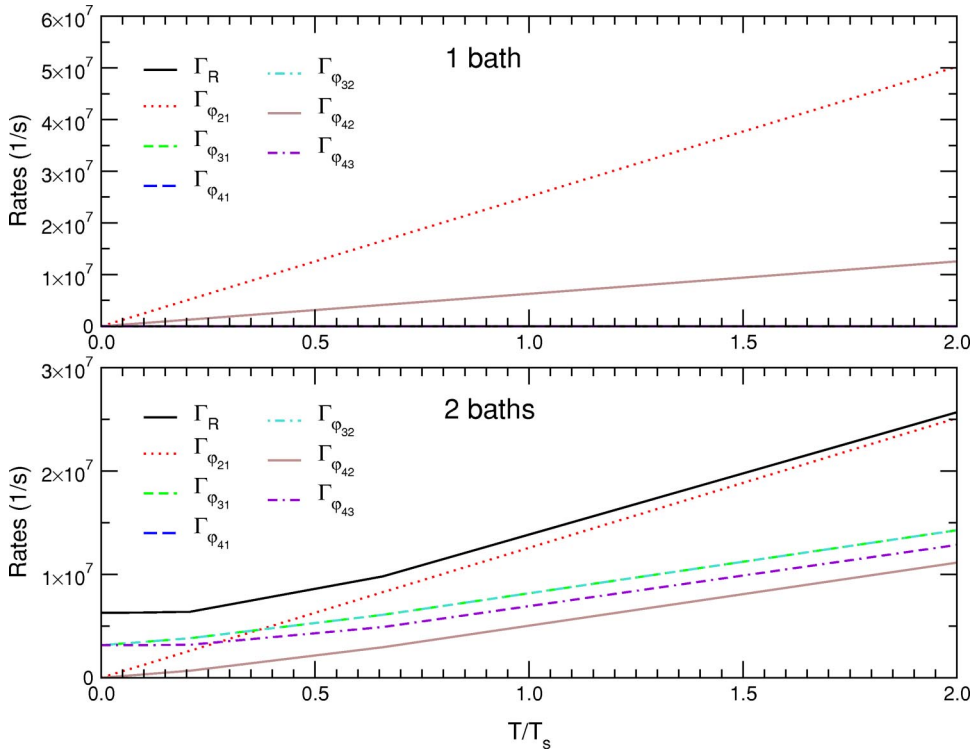
FIG. 9. Plot of the temperature dependence of the sum of the four relaxation rates and selected dephasing rates. Qubit parameters ϵ and η are set to 0, K is set to E_s, and $\alpha = 10^{-3}$ corresponding to the choice of parameters used for the U_{XOR} operation. The upper panel shows the case of one common bath and the lower panel the case of two distinct baths. In the case of one common bath the system will experience no dissipative effects at $T=0$.

field rates that depends on temperature. At temperature $T \approx 0.1 T_s$, the rates show a sharp increase for both cases. This roll-off point is set by the characteristic energy scale of the problem, which in turn is set by the energy bias ϵ, the transmission matrix element η, and the coupling strength K. For the choice of parameters in Fig. 8, the characteristic energy scale expressed in temperature is $T \approx 0.1 T_s$.

Note that there is also dephasing between the singlet and the triplet states. When the system is prepared (by application of a suitable interaction) in a coherent superposition of singlet and triplet states, the phase evolves coherently. Then two possible decoherence mechanisms can destroy phase coherence. First, "flipless" dephasing processes, where $\langle E \rangle$ remains unchanged. These flipless dephasing processes are described by the terms for $\omega_{\ell m}, \omega_{nk} \to 0$ in the rates, Eqs. (16) and (18). Obviously, these terms vanish for $T \to 0$, as the low-frequency component of Ohmic Gaussian noise is strictly thermal. Second, relaxation due to emission of a boson to the bath is also accompanied by a loss of phase coherence. This process in general has a *finite* rate at $T=0$. This explains the T dependence of the rates in the single-bath case: $|E1\rangle$ alone is protected from the environment. As there are incoherent transitions between the triplet eigenstates even at $T=0$, the relative phase of a coherent oscillation between $|E1\rangle$ and any of those is randomized, and the decoherence rates $\Gamma_{\varphi_{3/4,1}}$ are finite even at $T=0$. As a notable exception, $|E2\rangle$, the lowest-energy state in the triplet subspace, can only be flipped through absorption of energy, which implies that the dephasing rate $\Gamma_{\varphi_{21}}$ also vanishes at low temperature. The described behavior can be observed in Fig. 8.

If the parameters ϵ and η are tuned to zero, thus K being the only nonvanishing parameter in the Hamiltonian, all dephasing and relaxation rates will vanish for $T=0$ in the

case of one common bath. This behavior is depicted in Fig. 9. It originates from the special symmetries of the Hamiltonian in this case and the fact that for this particular two-qubit operation, the system Hamiltonian and the coupling to the bath are diagonal in the same basis. This special case is of crucial importance for the quantum gate operation as described in Sec. V and affects the gate quality factors.

E. Renormalization effects

Next to causing decoherence, the interaction with the bath also renormalizes the qubit frequencies. This is mostly due to the fast bath modes, and can be understood analogous to the Franck-Condon effect, the Lamb shift, or the adiabatic renormalization [30]. Renormalization of the oscillation frequencies ω_{nm} is controlled by the imaginary part of the Redfield tensor [16]

$$\omega_{nm} \to \tilde{\omega}_{nm} := \omega_{nm} - \mathrm{Im} R_{nmnm}. \tag{19}$$

Note that $\mathrm{Im} R_{nmnm} = -\mathrm{Im} R_{mnmn}$ due to the fact that the correlators in the Golden Rule expressions have the same parity. The imaginary part of the Redfield tensor is given by

$$\mathrm{Im} \Gamma^{(+)}_{\ell mnk} = C^{1b,2b}_{\ell mnk} \frac{1}{\pi \hbar} \mathcal{P} \int_0^\infty d\omega \, J(\omega) \left(\frac{1}{\omega^2 - \omega_{nk}^2} \right)$$
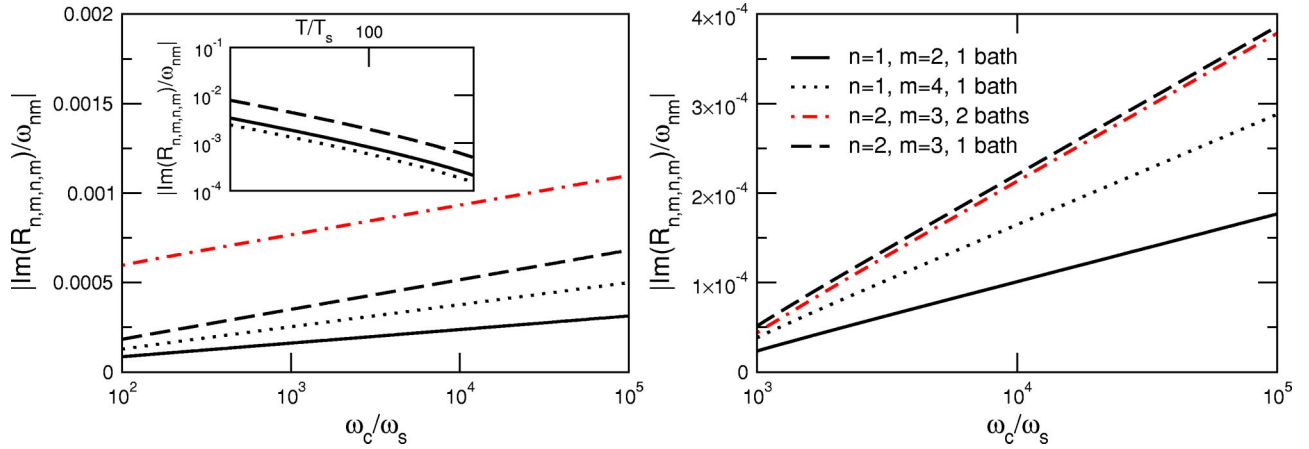$$\times [\coth(\beta \hbar \omega / 2) \omega_{nk} - \omega] \tag{20}$$

and

FIG. 10. The left plot depicts the ratio of the renormalization effects and the corresponding transition frequencies. Parameters: $\alpha = 10^{-3}$, $T=0$, and ω_c/ω_s is varied between 10^2 and 10^5 for several frequencies (ω_{12}, ω_{14}, and ω_{23}) for the case of two baths and in the case of ω_{23} also for the case of one common bath. The parameters for the right plot are $\alpha = 10^{-3}$, $T=2.1T_s$, and ω_c/ω_s is varied between 10^3 and 10^5. The inset of the left plot shows a log-log plot of the temperature dependence of the renormalization effects. Here $\alpha = 10^{-3}$ and $\omega_c = 10^{13}$. Note that for small temperatures the renormalization effects do *not* depend on temperature. (This is elucidated further in Sec. IV E.) The plots are scaled logarithmically to emphasize the logarithmic divergence of the renormalization effects with ω_c.

$$\mathrm{Im}\Gamma_{\ell mnk}^{(-)} = C_{\ell mnk}^{\mathrm{1b,2b}}\frac{1}{\pi\hbar}\mathcal{P}\int_0^\infty d\omega\, J(\omega)\left(\frac{1}{\omega^2-\omega_{\ell m}^2}\right)$$

$$\times[\coth(\beta\hbar\omega/2)\omega_{\ell m}+\omega], \qquad (21)$$

where $\mathcal{P}$ denotes the principal value, and $C_{\ell mnk}^{\mathrm{1b,2b}}$ are prefactors defined, in the case of two distinct baths, according to $C_{\ell mnk}^{\mathrm{2b}} = \frac{1}{4}[\sigma_{z,\ell m}^{(1)}\sigma_{z,nk}^{(1)}+\sigma_{z,\ell m}^{(2)}\sigma_{z,nk}^{(2)}]$ and in the case of one common bath $C_{\ell mnk}^{\mathrm{1b}} = \frac{1}{4}\Lambda$. Here, for simplicity, we assumed $\alpha_1 = \alpha_2 = \alpha$ and thus, $J_1(\omega) = J_2(\omega) = J(\omega)$. Evaluation of the integral leads to the following expression for $\Gamma_{\ell mnk}^{(+)}$:

$$\mathrm{Im}\Gamma_{\ell mnk}^{(+)} = C_{\ell mnk}^{\mathrm{1b,2b}}\frac{\alpha\omega_c^2\omega_{nk}}{2\pi(\omega_c^2+\omega_{nk}^2)}\left[\psi(1+c_2)+\psi(c_2)\right.$$

$$\left.-2\mathrm{Re}[\psi(ic_1)]-\pi\frac{\omega_c}{\omega_{nk}}\right], \qquad (22)$$

with $c_1 := (\beta\hbar\omega_{nk})/(2\pi)$ and $c_2 := (\beta\hbar\omega_c)/(2\pi)$. In the case of $\Gamma_{\ell mnk}^{(-)}$, the expression is

$$\mathrm{Im}\Gamma_{\ell mnk}^{(-)} = C_{\ell mnk}^{\mathrm{1b,2b}}\frac{\alpha\omega_c^2\omega_{\ell m}}{2\pi(\omega_c^2+\omega_{\ell m}^2)}\left[\psi(1+c_2)+\psi(c_2)\right.$$

$$\left.-2\mathrm{Re}[\psi(ic_1)]+\pi\frac{\omega_c}{\omega_{\ell m}}\right], \qquad (23)$$

with $c_1 := (\omega_{\ell m}\beta\hbar)/(2\pi)$. The terms in Eqs. (22) and (23) which are linear in ω_c give no net contribution to the imaginary part of the Redfield tensor [16]. To illustrate the size of the renormalization effects, the ratio of the renormalization effects to the frequencies which are renormalized is depicted in Fig. 10.

If c_1 and c_2 are large, and the digamma functions can be approximated by a logarithm, the resulting expression for the renormalization effects will be independent of temperature.

The temperature dependence of Eqs. (22) and (23) at higher temperatures, where c_1 and c_2 are small and the renormalization effects are very weak, is shown in Fig. 10. The rates (22) and (23) diverge logarithmically with ω_c in analogy to the well-known ultraviolet-divergence of the spin boson model [30]. When comparing the left ($T=0$) and right ($T=2.1T_s$) panel, one recognizes that for the first case, one common bath gives somewhat smaller renormalization effects than two distinct baths, while in the second case for $T=2.1T_s$, the renormalization effects deviate only slightly (see the behavior for ω_{23}) and the renormalization effects are smaller for the case of two distinct baths. The effects of renormalization are always very small $[|\mathrm{Im}(R_{n,m,n,m})/\omega_{nm}|$ below 1% for our choice of parameters] and are therefore, neglected in our calculations. However, having calculated Eqs. (22) and (23), these are easily incorporated in our numerical calculations. The case of large renormalization effects is discussed in Ref. [31].

We only plotted the size of the renormalization effects for ω_{12}, ω_{14}, and ω_{34}, because in general, all values of ω_{nk} are of the same magnitude and give similar plots. The size of the renormalization effects diverges linearly with α, the dimensionless parameter that describes the strength of the dissipative effects.

For flux qubits, the cutoff frequency ω_c is given by the circuit properties. For a typical first order low-pass LR filter [32] in a qubit circuit [13], one can insert $R=50\ \Omega$ (typical impedance of coaxial cables) and $L\approx 1$ nH (depends on the length of the circuit lines) into $\omega_{LR}=R/L$, and gets that $\omega_{LR}\approx 5\times 10^{10}$ Hz. ω_{LR} is the largest frequency in the problem (see again Ref. [13], Chap. 4.5) and $\omega_c\gg\omega_{LR}$ should hold. Then $\omega_c\approx 10^{13}$ Hz ($=10^4 E_s$) as cutoff frequency is a reasonable assumption.

V. GATE QUALITY FACTORS

In Sec. IV, we evaluated the dephasing and relaxation rates of the two-qubit system that is affected by a dissipative

environment. Furthermore, we visualized the dynamics of the two-qubit system. This does not yet allow a full assessment of the performance as a quantum logic element. These should perform unitary gate operations and based on the rates alone, one can not judge how well quantum gate operations might be performed with the two-qubit system. Therefore, to get a quantitative measure of how our setup behaves when performing a quantum logic gate operation, one can evaluate gate quality factors [33]. The performance of a two-qubit gate is characterized by four quantities: the fidelity, purity, quantum degree, and entanglement capability. The fidelity is defined as

$$\mathcal{F}=\frac{1}{16}\sum_{j=1}^{16}\langle\Psi_{in}^{j}|U_{G}^{+}\rho_{G}^{j}U_{G}|\Psi_{in}^{j}\rangle, \tag{24}$$

where U_{G} is the unitary matrix describing the desired ideal gate and the density matrix obtained from attempting a quantum gate operation in a hostile environment is $\rho_{G}^{j}=\rho(t_{G})$, which is evaluated for all initial conditions $\rho(0)=|\Psi_{in}^{j}\rangle\langle\Psi_{in}^{j}|$. The fidelity is a measure of how well a quantum logic operation was performed. Without dissipation, the reduced density matrix ρ_{G}^{j} after performing the quantum gate operation, applying U_{G} and the inverse U_{G}^{+} would equal $\rho(0)$. Therefore, the fidelity for the ideal quantum gate operation should be 1.

The second quantifier is the purity

$$\mathcal{P}=\frac{1}{16}\sum_{j=1}^{16}\mathrm{tr}((\rho_{G}^{j})^{2}), \tag{25}$$

which should be 1 without dissipation and 1/4 in a fully mixed state. The purity characterizes the effects of decoherence.

The third quantifier, the quantum degree, is defined as the maximum overlap of the resulting density matrix after the quantum gate operation with the maximally entangled states, the Bell states

$$\mathcal{Q}=\max_{j,k}\langle\Psi_{me}^{k}|\rho_{G}^{j}|\Psi_{me}^{k}\rangle, \tag{26}$$

where the Bell states Ψ_{me}^{k} are defined according to

$$|\Psi_{me}^{00}\rangle=\frac{|\downarrow\downarrow\rangle+|\uparrow\uparrow\rangle}{\sqrt{2}},\quad|\Psi_{me}^{01}\rangle=\frac{|\downarrow\uparrow\rangle+|\uparrow\downarrow\rangle}{\sqrt{2}}, \tag{27}$$

$$|\Psi_{me}^{10}\rangle=\frac{|\downarrow\downarrow\rangle-|\uparrow\uparrow\rangle}{\sqrt{2}},\quad|\Psi_{me}^{11}\rangle=\frac{|\downarrow\uparrow\rangle-|\uparrow\downarrow\rangle}{\sqrt{2}}. \tag{28}$$

For an ideal entangling operation, e.g., the controlled-NOT gate, the quantum degree should be one. The quantum degree characterizes nonlocality. It has been shown [34] that all density operators that have an overlap with a maximally entangled state that is larger than the value 0.78 [17] violate the Clauser-Horne-Shimony-Holt inequality and are thus nonlocal.

The fourth quantifier, the entanglement capability $\mathcal{C}$, is the smallest eigenvalue of the partially transposed density matrix for all possible unentangled input states $|\Psi_{in}^{j}\rangle$. (see below). It has been shown [35] to be negative for an entangled state. This quantifier should be -0.5, e.g., for the ideal U_{XOR}, thus characterizing a maximally entangled final state. Two of the gate quality factors, namely, the fidelity and purity might also be calculated for single-qubit gates [12]. However, entanglement can only be observed in a system of at least two qubits. Therefore, the quantum degree and entanglement capability cannot be evaluated for single-qubit gates.

To form all possible initial density matrices, needed to calculate the gate quality factors, we use the 16 unentangled product states $|\Psi_{in}^{j}\rangle$, $j=1,\ldots,16$ defined [17] according to $|\Psi_{a}\rangle_{1}|\Psi_{b}\rangle_{2}$ $(a,b=1,\ldots,4)$, with $|\Psi_{1}\rangle=|\downarrow\rangle$, $|\Psi_{2}\rangle=|\uparrow\rangle$, $|\Psi_{3}\rangle=(1/\sqrt{2})(|\downarrow\rangle+|\uparrow\rangle)$, and $|\Psi_{4}\rangle=(1/\sqrt{2})(|\downarrow\rangle+i|\uparrow\rangle)$. They form one possible basis set for the superoperator ν_{G} with $\rho(t_{G})=\nu_{G}\rho(0)$ [17,33]. The states are chosen to be unentangled for being compatible with the definition of $\mathcal{C}$.

A. Implementation of two-qubit operations

1. Controlled phase-shift gate

To perform the controlled-NOT operation, it is necessary to be able to apply the controlled phase-shift operation together with arbitrary single-qubit gates. In the computational basis $(|00\rangle,|01\rangle,|10\rangle,|11\rangle)$, the controlled phase-shift operation is given by

$$U_{CZ}(\varphi)=\begin{pmatrix}1&0&0&0\\0&1&0&0\\0&0&1&0\\0&0&0&e^{i\varphi}\end{pmatrix}, \tag{29}$$

and for $\varphi=\pi$, up to a global phase factor,

$$U_{CZ}=\exp\left(i\frac{\pi}{4}\sigma_{z}^{(1)}\right)\exp\left(i\frac{\pi}{4}\sigma_{z}^{(2)}\right)\exp\left(i\frac{\pi}{4}\sigma_{z}^{(1)}\sigma_{z}^{(2)}\right). \tag{30}$$

Note that in Eq. (30) only σ_{z} operations, which commute with the coupling to the bath, are needed. The controlled phase-shift operation together with two Hadamard gates and a single-qubit phase-shift operation then gives the controlled-NOT gate.

2. Controlled-NOT gate

Due to the fact that the set consisting of the U_{XOR} (or controlled-NOT) gate and the one-qubit rotations, is complete for quantum computation [36], the U_{XOR} gate is a highly important two-qubit gate operation. Therefore we further investigate the behavior of the four gate quality factors in this case. The U_{XOR} operation switches the second bit, depending on the value of the first bit of a two bit system. In the computational basis, this operation has the following matrix form:

TABLE I. Parameters of the Hamiltonians which are needed to perform the U_{XOR} gate operation; only the nonzero parameters are listed: $\xi = E_s$ in our case.

No.	Operation	Parameters (E_s)	Time (s)
1	$\exp\left[-i\frac{\pi}{2}\left(\frac{\sigma_x^2 + \sigma_z^2}{\sqrt{2}} \right) \right]$	$\epsilon_2 = -\xi,\ \Delta_2 = -\xi$	$\tau_1 = \frac{\sqrt{2}}{2\xi}$
2	$\exp\left(i\frac{\pi}{2}\sigma_z^1 \right)$	$\epsilon_1 = \xi$	$\tau_2 = \frac{1}{2\xi}$
3	$\exp\left(i\frac{\pi}{4}\sigma_z^1 \sigma_z^2 \right)$	$K = \xi$	$\tau_3 = \frac{1}{4\xi}$
4	$\exp\left(i\frac{\pi}{4}\sigma_z^2 \right)$	$\epsilon_2 = \xi$	$\tau_4 = \frac{1}{4\xi}$
5	$\exp\left(i\frac{\pi}{4}\sigma_z^1 \right)$	$\epsilon_1 = \xi$	$\tau_5 = \frac{1}{4\xi}$
6	$\exp\left[-i\frac{\pi}{2}\left(\frac{\sigma_x^2 + \sigma_z^2}{\sqrt{2}} \right) \right]$	$\epsilon_2 = -\xi,\ \Delta_2 = -\xi$	$\tau_6 = \frac{\sqrt{2}}{2\xi}$

$$U_{XOR} = \begin{pmatrix} 1 & 0 & 0 & 0 \\ 0 & 1 & 0 & 0 \\ 0 & 0 & 0 & 1 \\ 0 & 0 & 1 & 0 \end{pmatrix}. \qquad (31)$$

Up to a phase factor, the two-qubit U_{XOR} (or CNOT) operation can be realized by a sequence of five single-qubit and one two-qubit quantum logic operations. Each of these six operations corresponds to an appropriate Hamiltonian undergoing free unitary time evolution $\exp[-(i/\hbar)\mathbf{H}_{op}t]$. The single-qubit operations are handled with Bloch-Redfield formalism, like the two-qubit operations. We assume dc pulses (instantaneous on and off switching of the Hamiltonian with zero rise time of the signal) or rectangular pulses

$$U_{XOR} = \exp\left[-i\frac{\pi}{2}\left(\frac{\sigma_x^{(2)} + \sigma_z^{(2)}}{\sqrt{2}} \right) \right] U_{CZ}(\pi)$$
$$\times \exp\left(i\frac{\pi}{2}\sigma_z^{(1)} \right) \exp\left[-i\frac{\pi}{2}\left(\frac{\sigma_x^{(2)} + \sigma_z^{(2)}}{\sqrt{2}} \right) \right],$$
$$(32)$$

where $U_{CZ}(\pi)$ is given by Eq. (30). This generic implementation has been chosen in order to demonstrate the comparison to other coupling schemes [17] as well as for computational convenience, it is not necessarily the optimum scheme for application under cryogenic conditions, where slow rise-time ac pulses are preferred. Table I shows the parameters we inserted into the one- and two-qubit Hamiltonian to receive the U_{XOR} operation. In our case, we assumed $\xi = E_s$. However, there is no restriction in the use of other values for ξ. For a typical energy scale of 1 GHz, the resulting times from Table I are in the nanosecond range.

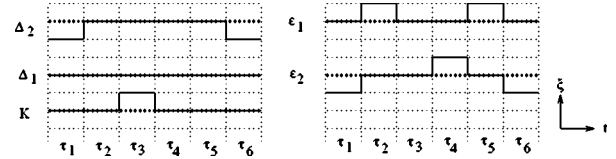To better visualize the pulse sequence needed to perform the quantum U_{XOR} operation, which was already given in

FIG. 11. Pulse sequence needed to perform the quantum U_{XOR} operation. Here, the elements of the unperturbed single- and two-qubit Hamiltonian needed to perform a certain operation undergoing free unitary time evolution are shown. The dotted horizontal lines denote $\xi = 0$, and the horizontal lines are spaced by $|\xi| = E_s$. The durations of each pulse are not equal in general $\tau_j \neq \tau_i$, $i,j = 1, \ldots, 6$ (cf. Table I).

Table I, Fig. 11 depicts the values of the elements of the Hamiltonians. Interestingly enough, we find that for the only two-qubit operation included in the U_{XOR} operation, ϵ and η are zero. Thus, K is the only nonzero parameter and $\mathbf{H}_{2qb}$ assumes diagonal form. For flux qubits, implementing the pulse sequence Fig. 11 involves negative and positive values tuning the magnetic frustration through the qubit loop below or above $f = 1/2$. Note that, e.g., for realistic models of inductively coupled flux qubits, it is very difficult to turn on the interaction Hamiltonian between the two qubits without the individual σ_z terms in the Hamiltonian. However, for the pulse sequence given in Eq. (32), we might simply perform the third, fourth, and fifth operations of Eq. (32) at once using only the Hamiltonian with both the individual σ_z terms and the interqubit coupling.

To obtain the final reduced density matrix after performing the six unitary operations (32), we iteratively determine the density matrix after each operation with Bloch-Redfield theory and insert the attained resulting density matrix as initial density matrix into the next operation. This procedure is repeated for all possible unentangled initial states given in the preceding section. We inserted no additional time intervals between the operations. This is usually needed, if one applies Bloch-Redfield formalism, because it is known to violate complete positivity on short time scales. However, we circumvent this problem in our calculations by dropping the memory after each operation, when we iteratively calculate the reduced density matrix. This procedure may lead to small inaccuracies as compared to using QUAPPI [17], which, however, should not affect our main conclusions.

B. Temperature dependence

1. Controlled phase-shift gate

We have analyzed the gate quality factors in the cases of a common and of two distinct baths, respectively. In Fig. 12, the temperature dependence of the deviations of the four gate quality factors from their ideal values are depicted as a log-log plot. At temperatures below $T = 2.5 \times 10^{-2}$ K $\approx 0.5 T_s$, the purity and fidelity are clearly higher for the case of one common bath, but if temperature is increased above this characteristic threshold, fidelity and purity are slightly higher for the case of two baths.

In the case of one common bath the fidelity, purity, and entanglement capability are approaching their ideal value 1,
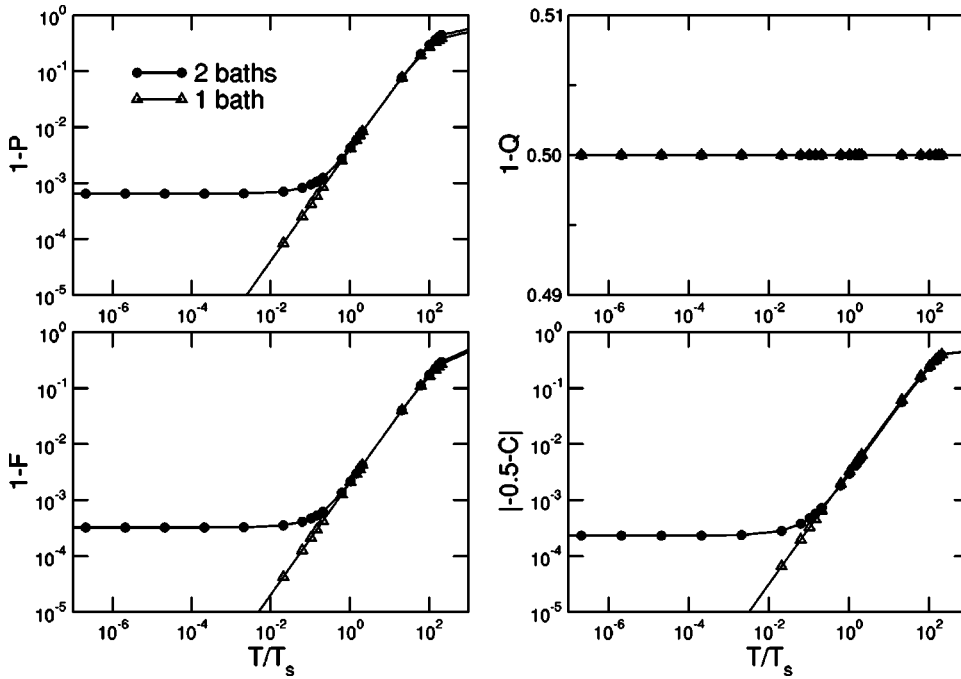
FIG. 12. Log-log plot of the temperature dependence of the deviations of the four gate quantifiers from their ideal values after performing the controlled phase-shift (CPHASE) gate operation. In all cases, $\alpha = \alpha_1 = \alpha_2 = 10^{-3}$. The full curves are provided as guides to the eye.

when temperature goes to zero. This is related to the fact that in the case of one common bath all relaxation and dephasing rates vanish during the two-qubit step of the controlled phase-shift gate due to the special symmetries of the Hamiltonian, when temperature goes to zero as depicted in Fig. 9.

The controlled phase-shift operation creates entanglement. The creation of entanglement is impeded by decoherence effects that vanish when temperature approaches zero. Therefore, the entanglement capability exhibits the same behavior as the fidelity and purity. For zero dissipation ($\alpha = 0$), the quantum degree has the value 0.5 but the entanglement capability is -0.5 thus, characterizing a maximum entangled state. The reason is that the Bell-states, which are generated by the controlled phase-shift gate from the input states, result in a basis that is different from the used basis, but can be transformed using only local transformations.

Furthermore, for finite dissipation, Fig. 9 shows that also for the case of two distinct baths, there are only three non-vanishing rates for $T \rightarrow 0$. The system, being prepared in one of the 16 initial states, might relax into one of the eigenstates that is an entangled state.

We observe the saturation of the deviation for the case of two baths and can directly recognize the effects of the symmetries of the controlled phase-shift operation. For given α, the fidelity and purity cannot be increased anymore by lowering the temperature in the case of two distinct baths. Interestingly enough, we find that for two qubits coupling to one common bath, the situation is different for temperatures below $0.5T_s$. Above a temperature of $T_s = 4.8 \times 10^{-2}$ K, the decrease of the gate quality factors shows a linear dependence on temperature for both cases of one common or two distinct heat baths before it again saturates at about 10^2 K $\approx 2 \times 10^3 T_s$. Finite decoherence effects in the fidelity, purity and entanglement capability at $T = 0$ for the case of two distinct baths are resulting from the coupling of the system to the environment of harmonic oscillators, which (at $T = 0$) are

all in their ground states and can be excited through spontaneous emission. But for the case of one common bath, the deviation from the ideal fidelity goes to zero, when temperature goes to zero. This is due to the special symmetries (K is the only *non*vanishing parameter in the two-qubit operation) of the Hamiltonian, which rules out spontaneous emission. These symmetries are also reflected in the temperature dependence of the rates, Fig. 9. There, for one common bath, all rates vanish for $T \rightarrow 0$. Note that these rates only describe the two-qubit part of the operation. However, the single-qubit part behaves similarly, because the terms in the single-qubit Hamiltonian are also $\propto \sigma_z$.

2. Controlled-NOT gate

Different to the preceding section, we now add two single-qubit operations (Hadamard gates) to the controlled phase-shift operation that do *not* commute with the coupling to the bath. In Fig. 13, the deviations of the gate quality factors from their ideal values are depicted as a log-log plot. Again, at temperatures below $T = 2.5 \times 10^{-2}$ K $\approx 0.5T_s$, the purity and fidelity are higher for the case of one common bath, but if temperature is increased above this characteristic threshold, fidelity and purity are higher for the case of two baths. Note that, we have chosen a rather large α, this value can substantially be improved by means of engineering [13]. The fidelity and purity are clearly higher for the case of one common bath, when temperature is decreased below $0.5T_s$. This is related to the fact that in the case of one common bath, all relaxation and dephasing rates vanish during the two-qubit-step of the U_{XOR}, due to the special symmetries of the Hamiltonian, when temperature goes to zero as discussed in the preceding paragraph. However, the quantum degree and the entanglement capability tend towards the same value for both the case of one common and two distinct baths. This is due to the fact that both quantum degree and entanglement capability are, different than fidelity and purity, not defined
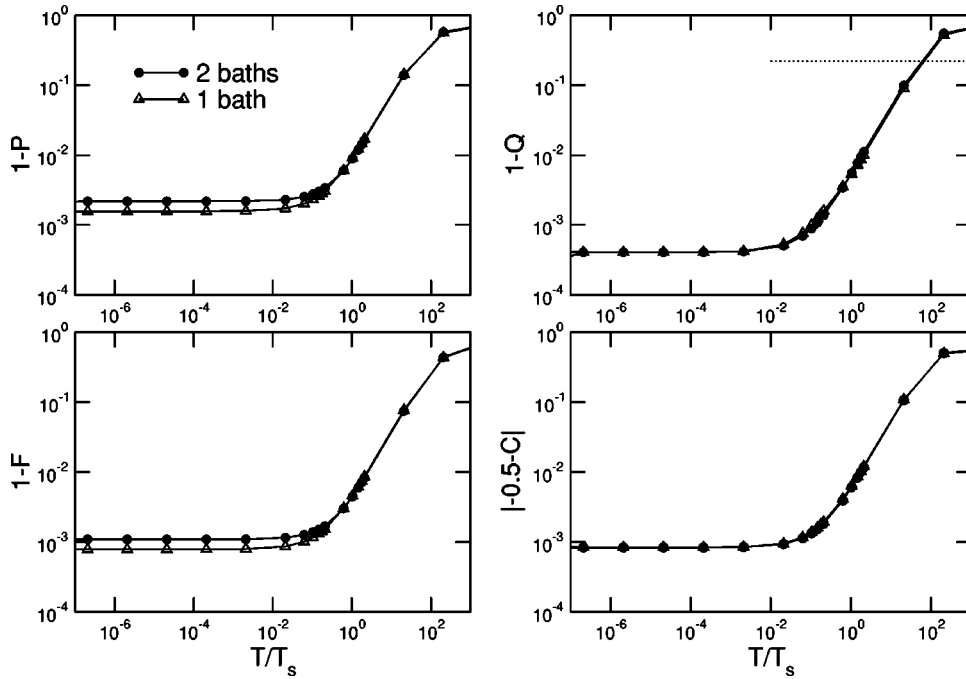
FIG. 13. Log-log plot of the temperature dependence of the deviations of the four gate quantifiers from their ideal values after performing the U_{XOR} gate operation. In all cases, $\alpha = \alpha_1 = \alpha_2 = 10^{-3}$. The dotted line indicates the upper bound set by the Clauser-Horne-Shimony-Holt inequality. The full curves are provided as guides to the eye.

as mean values but rather characterize the "best" possible case of all given input states. This results in the same value for both cases.

In the recent work by Thorwart and Hänggi [17], the U_{XOR} gate was investigated for a $\sigma_y^{(i)} \otimes \sigma_y^{(j)}$ coupling scheme and one common bath. They find a pronounced degradation of the gate performance, in particular, the gate quality factors only weakly depend on temperature. They set the strength of the dissipative effects to $\alpha = 10^{-4}$. Their choice of parameters was $\epsilon \approx 10 E_s$, $\Delta \approx 1 E_s$, and $K \approx 0.5 E_s$ which is on the same order of magnitude as the values given in Table I. As can be seen in Fig. 13, we also observe only a weak decrease of the gate quality factors for both the cases of one common bath and two distinct baths in the same temperature range discussed by Thorwart and Hänggi, both for $\alpha = 10^{-3}$ and $\alpha = 10^{-4}$ and overall substantially better values. This is due to the fact that for $\sigma_y^{(i)} \otimes \sigma_y^{(j)}$ coupling, the Hamiltonian does *not* commute with the coupling to the bath during the two-qubit steps of the U_{XOR} pulse sequence.

We observe the saturation of the deviation for both the cases of two baths and one common bath. For given α, the fidelity and purity can not be increased anymore by lowering the temperature, different from the behavior for the controlled phase-shift gate that was discussed in the preceding section. This is due to the application of the Hadamard gate whose Hamiltonian does not commute with the coupling to the bath. Above a temperature of T_s, the decrease of the gate quality factors shows a linear dependence on temperature for both cases. Here, different from the controlled phase-shift gate, we observe finite decoherence effects in all four gate quantifiers also at $T = 0$, both for the case of one common or two distinct heat baths. These decoherence effects are resulting from the coupling of the system to the environment of harmonic oscillators, which (at $T = 0$) are all in their ground states and can be excited through spontaneous emission as already described above.

The dotted line in Fig. 13 shows that the temperature has to be less than about $T = 21 T_s = 1$ K in order to obtain values of the quantum degree being larger than $\mathcal{Q} \approx 0.78$. Only then, the Clauser-Horne-Shimony-Holt inequality is violated and nonlocal correlations between the qubits occur as described in Ref. [17].

C. Dependence on the dissipation strength

The deviations from the ideal values of the gate quantifiers possess a linear dependence on α as expected. Generally (if no special symmetries of the Hamiltonian are present), there are always finite decoherence effects also at $T = 0$. Therefore, we can not improve the gate quality factors below a certain saturation value, when lowering the temperature [17], as was also discussed in the preceding section. By better isolating the system from the environment and by carefully engineering the environment [13], one can decrease the strength of the dissipative effects characterized by α. In order to obtain the desired value of 0.999 99 for $\mathcal{F}$, $\mathcal{P}$, and $\mathcal{Q}$ [17], α needs to be below 10^{-6} at $T = 0.21 T_s = 10$ mK.

D. Time resolved controlled-NOT operation

To investigate the anatomy of the U_{XOR} quantum logic operation, we calculated the occupation probabilities of the singlet/triplet states after each of the six operations, of which the U_{XOR} consists. This time resolved picture of the dynamics of the two-qubit system, when performing a gate operation, gives insight into details of our implementation of the U_{XOR} operation and the dissipative effects that occur during the operation. Thus, we are able to characterize the physical process, which maps the input density matrix ρ_0 to ρ_{out} in an open quantum system [33]. When the system is prepared in the state $|\downarrow\downarrow\rangle = |00\rangle$, the U_{XOR} operation (31) does not alter the initial state and after performing the U_{XOR} operation, the final state should equal the initial state $|\downarrow\downarrow\rangle = |00\rangle$. This can
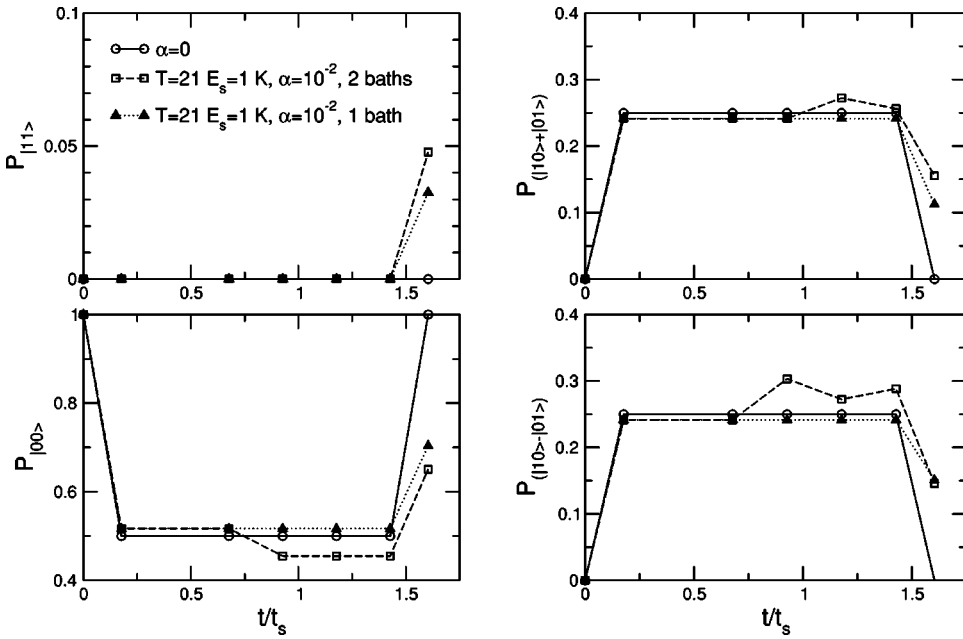
FIG. 14. Time resolved U_{XOR} operation. The system is initially prepared in the state $|00\rangle$. Occupation probabilities of the singlet/triplet states are shown after completion of a time step τ_i ($i = 1, \ldots, 6$). For $\alpha = \alpha_1 = \alpha_2 = 10^{-2}$ and $T = 21T_s = 1$ K clear deviations from the ideal case can be observed. Qubit parameters are set according to Table I. The lines are provided as guides to the eye.

clearly be observed in Fig. 14. During the U_{XOR} operation, occupation probabilities of the four states change according to the individual operations given in Eq. (32). At $T = 21T_s$, the case of two baths differs significantly from the case of one common bath. After the third operation (the two-qubit operation; only there the distinction between one common or two distinct baths makes sense), occupation probabilities are different for both environments resulting in a less ideal result for the case of two baths.

In Fig. 14, the resulting state after performing the U_{XOR} operation always deviates more from the ideal value (for $\alpha = 0$, i.e., no dissipation) for the case of two distinct baths, if all other parameters are fixed and set to the same values for both cases. The state $P_{|00\rangle}$ is less close to the ideal occupation probability one and the other singlet/triplet states are

also less close to their ideal value for the case of two distinct baths. The case of two distinct baths also shows bigger deviations from the ideal case ($\alpha = 0$) *during* the U_{XOR} operation (see Fig. 14). But, if the system is initially prepared in the state $|\uparrow\uparrow\rangle = |11\rangle$, the case of two distinct baths shows bigger deviations from the ideal case during the U_{XOR} operation, while the resulting state is closer to the ideal case for two distinct baths compared to one common bath.

In Figs. 14 and 15, it looks like there would be no decoherence effects (or at least much weaker decoherence effects) after performing the (first two) single-qubit operations. However, not all input states are affected by the decoherence effects the same way. And when we regard all possible input states, there are finite decoherence effects. This can be explained with Fig. 16. Figure 16 depicts the time resolved
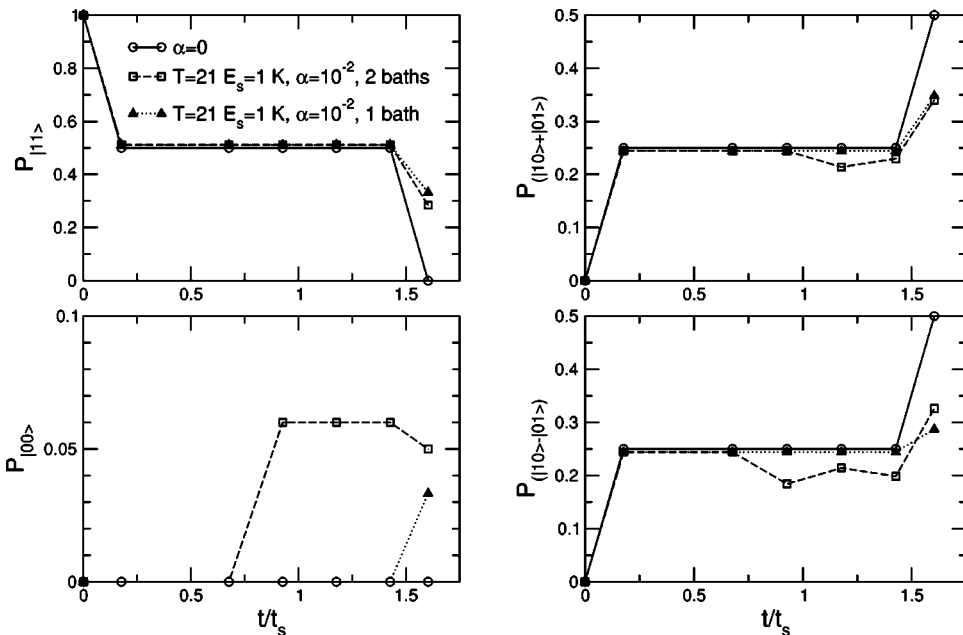

FIG. 15. Time resolved U_{XOR} operation. The system is initially prepared in the state $|11\rangle$. Occupation probabilities of the singlet/triplet states are shown after completion of a time step τ_i ($i = 1, \ldots, 6$). For $\alpha = \alpha_1 = \alpha_2 = 10^{-2}$ and $T = 21T_s = 1$ K, deviations from the ideal case can be observed. Qubit parameters are set according to Table I. The lines are provided as guides to the eye.
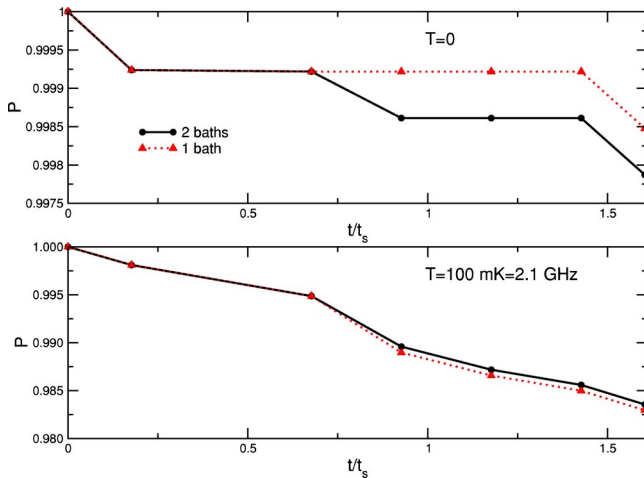
FIG. 16. Time resolved purity for the U_{XOR} operation. The value of the purity after each time step τ_i ($i = 1, \ldots, 6$) is shown. Here $\alpha = \alpha_1 = \alpha_2 = 10^{-2}$, and $T = 2.1 T_s = 100$ mK (lower panel) or $T = 0$ (upper panel). Qubit parameters are set according to Table I. The lines are provided as guides to the eye.

purity when performing the U_{XOR} operation. We clearly observe that there are finite decoherence effects for the first single-qubit operations in Eq. (32) as well. The difference between the single-qubit and two-qubit operations is the steeper decrease of the purity due to stronger decoherence in the case of the two-qubit operation. The upper panel in Fig. 16 depicts the behavior of the purity for $T \rightarrow 0$. Decoherence due to the σ_z terms in the Hamiltonian will vanish for $T \rightarrow 0$ in the case of one common bath.

VI. CONCLUSION

We presented a full analysis of the dynamics and decoherence properties of two solid-state qubits coupled to each other via a generic type of Ising coupling and coupled, moreover, either to a common bath, or two independent baths.

We calculated the dynamics of the system and evaluated decoherence times. From the temperature dependence of the decoherence rates (Fig. 8), we conclude that both types of environments show a similar behavior; however, in the case of one common bath, two of the decoherence rates are zero, and the remaining ones are slightly larger than in the case of two distinct baths. This temperature dependence is also reflected in the characteristics of the gate quality factors from quantum information theory, which are introduced as robust

measures of the quality of a quantum logic operation. We illustrate that the gate quality factors depend linearly on α, as expected. The time resolved U_{XOR} operation (Figs. 14 and 15) again illustrates the difference between one common and two distinct baths, and moreover, we observe that single-qubit decoherence effects $\propto \sigma_z$ during the U_{XOR} operation are weak. The time scales of the dynamics of the coupled two qubit system are comparable to the time scales, which were already observed in experiments and discussed in the literature [13].

The question, whether one common bath or two distinct baths are less destructive regarding quantum coherence can not be clearly answered. For low enough temperatures, coupling to one common bath yields better results. However, when the temperature is increased, two distinct baths do better; in both temperature regimes, though, the gate quantifiers are only slightly different for both cases.

Compared to the work of Thorwart [17], the interaction part of our model Hamiltonian possesses symmetries (the Hamiltonian of the two-qubit operation and the errors commute) that lead to better gate quality factors. Furthermore, analysis of the symmetries and error sources of our model system can lead to improved coupling schemes for solid-state qubits. Milburn and co-workers on the other hand focused on comparison of classical and quantum mechanical dynamics [15] and estimated the decoherence properties of two coupled two-state systems.

Governale [16] determined the decoherence properties of two coupled charge qubits whose Hamiltonian differs from Eq. (2) by the type of interqubit coupling, namely, $\sigma_y^{(1)} \otimes \sigma_y^{(2)}$ coupling. However, introducing the quality factors gives a measure to judge how certain qubit designs perform quantum gate operations.

As a next step, one should consider driving, to be able to observe and discuss Rabi oscillations in systems of two coupled qubits. It should be investigated, how the decoherence properties are modified, if one adds more qubits to the system.

[1] P. Shor, in *Proceedings of 35th Annual Symposium on the Foundations of Computer Science*, edited by S. Goldwasser (IEEE Computer Society Press, Los Alamitos, 1994), pp. 124–134.

[2] L.K. Grover, Phys. Rev. Lett. **79**, 325 (1997).

[3] D. Deutsch, Proc. R. Soc. London, Ser. A **400**, 97 (1985).

[4] D.P. DiVincenzo, Science **269**, 225 (1995).

[5] B.E. Kane, Nature (London) **393**, 133 (1998).

[6] T.P. Orlando *et al.*, Phys. Rev. B **60**, 15 398 (2000); J.E. Mooij *et al.*, Science **285**, 1036 (1999).

[7] Yu.A. Pashkin, T. Yamamoto, O. Astafiev, Y. Nakamura, D.V. Averin, and J.S. Tsai, Nature (London) **421**, 823 (2003).

[8] Y. Nakamura, Yu.A. Pashkin, and J.S. Tsai, Nature (London) **398**, 786 (2002).

[9] J.R. Friedman, V. Patel, W. Chen, S.K. Tolpygo, and J.E. Lukens, Nature (London) **406**, 43 (2000).

[10] D. Vion, A. Aassime, A. Cottet, P. Joyez, H. Pothier, C. Urbina, D. Esteve, and M.H. Devoret, Science **296**, 886 (2002).

[11] Y. Nakamura (private communication).

[12] M.C. Goorden, Masters thesis, Delft University of Technology, 2002 (unpublished); M.C. Goorden and F.K. Wilhelm (unpublished).

[13] C.H. van der Wal, *Quantum Superpositions of Persistent Josephson Currents* (Delft University Press, Delft, 2001); C.H. van der Wal, F.K. Wilhelm, C.J.P.M. Harmans, and J.E. Mooij, Eur. Phys. J. B **31**, 111 (2003).

[14] Y. Makhlin, G. Schön, and A. Shnirman, Rev. Mod. Phys. **73**, 357 (2001).

[15] G.J. Milburn, R. Laflamme, B.C. Sanders, and E. Knill, Phys. Rev. A **65**, 032316 (2002).

[16] M. Governale, M. Grifoni, and G. Schön, Chem. Phys. **268**, 273 (2001).

[17] M. Thorwart and P. Hänggi, Phys. Rev. A **65**, 012309 (2002).

[18] F.K. Wilhelm and J.E. Mooij (unpublished).

[19] R.H. Blick and H. Lorenz, in ISCAS 2000 Proceedings (unpublished), pp. II245-II248.

[20] J.B. Majer (private communication).

[21] D.A. Lidar, I.L. Chuang, and K.B. Whaley, Phys. Rev. Lett. **81**, 2594 (1998).

[22] J. Kempe, D. Bacon, D.A. Lidar, and K.B. Whaley, Phys. Rev. A **63**, 042307 (2001).

[23] M.J. Storcz, Masters thesis, University of Bonn, 2002 (unpublished).

[24] K. Segall *et al.*, IEEE Trans. Appl. Supercond. (to be published).

[25] C.H. van der Wal *et al.*, Science **290**, 773 (2000).

[26] P.N. Argyres and P.L. Kelley, Phys. Rev. **134**, A98 (1964).

[27] L. Hartmann, I. Goychuk, M. Grifoni, and P. Hänggi, Phys. Rev. E **61**, R4687 (2000); L. Hartmann, *Driven Tunneling Dynamics of Dissipative Two-State Quantum Systems* (Shaker Verlag, Aachen, 2000).

[28] U. Weiss, *Quantum Dissipative Systems*, 2nd ed. (World Scientific, Singapore, 1999).

[29] K. Blum, *Density Matrix Theory and Applications*, 1st ed. (Plenum, New York, 1981).

[30] A.J. Leggett *et al.*, Rev. Mod. Phys. **59**, 1 (1987).

[31] S. Kehrein and M. Vojta, e-print cond-mat/0208390.

[32] P. Horowitz and W. Hill, *The Art of Electronics*, 2nd ed. (Cambridge University Press, Cambridge, 1989).

[33] J.F. Poyatos, J.I. Cirac, and P. Zoller, Phys. Rev. Lett. **78**, 390 (1997).

[34] C.H. Bennett, G. Brassard, S. Popescu, B. Schumacher, J.A. Smolin, and W.K. Wootters, Phys. Rev. Lett. **76**, 722 (1996); J.F. Clauser, M.A. Horne, A. Shimony, and R.A. Holt, *ibid.* **23**, 880 (1969).

[35] A. Peres, Phys. Rev. Lett. **77**, 1413 (1996).

[36] A. Barenco, C.H. Bennett, R. Cleve, D.P. DiVincenzo, N. Margolus, P. Shor, T. Sleator, J.A. Smolin, and H. Weinfurter, Phys. Rev. A **52**, 3457 (1995).